Determination of the chiral indices (*n*,*m*) of carbon nanotubes by electron diffraction

Lu-Chang Qin

Received 28th September 2006, Accepted 19th October 2006
First published as an Advance Article on the web 22nd November 2006
DOI: 10.1039/b614121h

The atomic structure of a carbon nanotube can be defined by the chiral indices, (*n*,*m*), that specify its perimeter vector (chiral vector), with which the diameter and helicity are also determined. The fine electron beam available in a modern Transmission Electron Microscope (TEM) offers a unique and powerful probe to reveal the atomic structure of individual nanotubes. This article covers two aspects related to the use of the electron probe in the TEM for the study of carbon nanotubes: (i) to express the electron diffraction intensity distribution in the electron diffraction patterns of carbon nanotubes and (ii) to obtain the chiral indices (*n*,*m*) of carbon nanotubes from their electron diffraction patterns. For a nanotube of given chiral indices (*n*,*m*), the electron scattering amplitude from the carbon nanotube can be expressed analytically in closed form using the helical diffraction theory, from which its electron diffraction pattern can be calculated and understood. The reverse problem, *i.e.*, assignment of the chiral indices (*n*,*m*) of a carbon nanotube from its electron diffraction pattern, is approached from the relationship between the electron diffraction intensity distribution and the chiral indices (*n*,*m*). The first method is to obtain indiscriminately the chiral indices (*n*,*m*) by reading directly the intensity distribution on the three principal layer lines, l_1, l_2, and l_3, which have intensities proportional to the square of the Bessel functions of orders *m*, *n*, and $n + m$: $I_{l1} \propto |J_m(\pi dR)|^2$, $I_{l2} \propto |J_n(\pi dR)|^2$, and $I_{l3} \propto |J_{n+m}(\pi dR)|^2$. The second method is to obtain and use the ratio of the indices $n/m = (2D_1 - D_2)/(2D_2 - D_1)$ in which D_1 and D_2 are the spacings of principal layer lines l_1 and l_2, respectively. Examples of using these methods are also illustrated in the determination of chiral indices of isolated individual single-walled carbon nanotubes, a bundle of single-walled carbon nanotubes, and multi-walled carbon nanotubes.

Introduction

Diamond and graphite have long been regarded as the only allotropes of crystalline carbon and their atomic structures were determined soon after the X-ray diffraction method was developed in the early 1910's.[1–3] The discovery of fullerenes and the subsequent success in their large scale synthesis prompted renewed searches of unknown structures of carbon at the nanometer scale.[4,5] Carbon nanotubes were first identified by Iijima in 1991[6] in the cathodic deposits produced by dc arc-discharge of two graphite electrodes in an apparatus developed to produce fine particles and fullerenes.[7] The ultimate form of carbon nanotubes is single-walled carbon nanotubes,[8,9] which can be constructed schematically by rolling up a rectangular cut of graphene about a chosen axis to form a seamless cylinder of diameter on the nanometer scale.

The atomic structure of a single-walled carbon nanotube is well described by its chiral indices (*n*,*m*) that specify the perimeter of the carbon nanotube on the graphene net. The determination of the chiral indices has been a challenge to researchers ever since carbon nanotubes were discovered. Transmission Electron Microscopy (TEM) has been the most powerful and most popular technique in characterizing the morphology and structure of carbon nanotubes. In addition to the TEM method, other analytical techniques, especially Raman spectroscopy,[10,11] optical absorption spectroscopy,[12,13] and scanning tunneling microscopy[14–18] have also been used extensively in attempt to elucidate the atomic structure and to obtain the chiral indices of carbon nanotubes. However, due to various limitations, there are still formidable difficulties to determine the atomic structure of carbon nanotubes accurately with these techniques.

Electron diffraction was the first technique employed to identify the helical nature in the structure of carbon nanotubes[6] and it has continued to play a vital role in the structural studies of carbon nanotubes. Based on the helical theory developed for the study of α-helix and the helical DNA molecules,[19–25] the kinematical diffraction theory for the scattering of electrons or X-rays from carbon nanotubes was formulated by Qin in 1994[26] and subsequently by Lucas *et al.* in 1996.[27–29] In addition, electron diffraction from carbon nanotubes was also discussed extensively using geometric illustrations.[30–35] On the other hand, electron diffraction has also been explored for the possibility of solving the atomic structure of carbon nanotubes, in particular, to obtain

W.M. Keck Laboratory for Atomic Imaging and Manipulation, Department of Physics and Astronomy, and Curriculum in Applied and Materials Sciences, University of North Carolina, Chapel Hill, NC 27599-3255, USA. E-mail: lcqin@physics.unc.edu

the helicity of carbon nanotubes over the past fifteen years.[36–46] Two approaches have been developed: one using a correction factor to obtain the chiral angle from the electron diffraction pattern,[39] and the other using the ratio of the layer lines measured in the electron diffraction patterns.[45] The atomic structure of a double-walled carbon nanotube was also obtained by an electron crystallographic method using phase retrieval.[47] Most recently, a one-step direct method has been developed[48] and has been applied to determine the atomic structure of a large number of carbon nanotubes, both single- and multi-walled.[49–51] Electron diffraction is by far the most powerful technique for studying the atomic structure, including the handedness, of carbon nanotubes with high accuracy, as can be seen in the literature.[52–85]

Structural description of carbon nanotubes

The solid state physics convention is used in this article to describe the graphene lattice structure, where the basis vectors of the graphene net, $\vec{a}_1$ and $\vec{a}_2$ ($a_1 = a_2 = a_0 = 0.246$ nm), are separated with an inter-angle of 60°, as shown schematically in Fig. 1(a) in radial projection. On the graphene net, the chiral indices (*n*,*m*) specify the perimeter of the carbon nanotube, as shown schematically in Fig. 1(a) for the chiral vector (7,1). For a carbon nanotube of given chiral indices (*n*,*m*), its perimeter vector is

$$\vec{A} = (n, m) = n\vec{a}_1 + m\vec{a}_2, \tag{1}$$

which has a magnitude $A = a_0(n^2 + m^2 + nm)^{1/2}$. The diameter, *d*, of the carbon nanotube is

$$d = \frac{A}{\pi} = \frac{a_0}{\pi}\sqrt{n^2 + m^2 + nm} \tag{2}$$

and the helicity, α, defined as the angle between the perimeter vector, $\vec{A} = (n,m)$, and the basis vector, $\vec{a}_1$, illustrated in Fig. 1(a), is

$$\begin{aligned} \alpha &= \cos^{-1}\left(\frac{2n+m}{2\sqrt{n^2+m^2+nm}}\right) \\ &= \sin^{-1}\left(\frac{\sqrt{3}m}{2\sqrt{n^2+m^2+nm}}\right) \\ &= \tan^{-1}\left(\frac{\sqrt{3}m}{2n+m}\right). \end{aligned} \tag{3}$$

Once the chiral indices (*n*,*m*) of a carbon nanotube are assigned, the tubule axis, (n_c,m_c), perpendicular to the chiral vector, $\vec{A}$, can be calculated by applying the orthogonality relationship between the tubule perimeter and the tubule axis, which yields

$$\frac{m_c}{n_c} = -\frac{2n+m}{n+2m}. \tag{4}$$

The indices of the tubule axis (n_c,m_c) should be chosen as the pair which has no common factors other than 1. Denoting *M* as the greatest common integer divisor of integers ($2n + m$) and ($n + 2m$), the axial lattice vector (n_c,m_c) can then be expressed as

$$\begin{cases} n_c = -\dfrac{n+2m}{M} \\ m_c = \dfrac{2n+m}{M} \end{cases}, \tag{5}$$

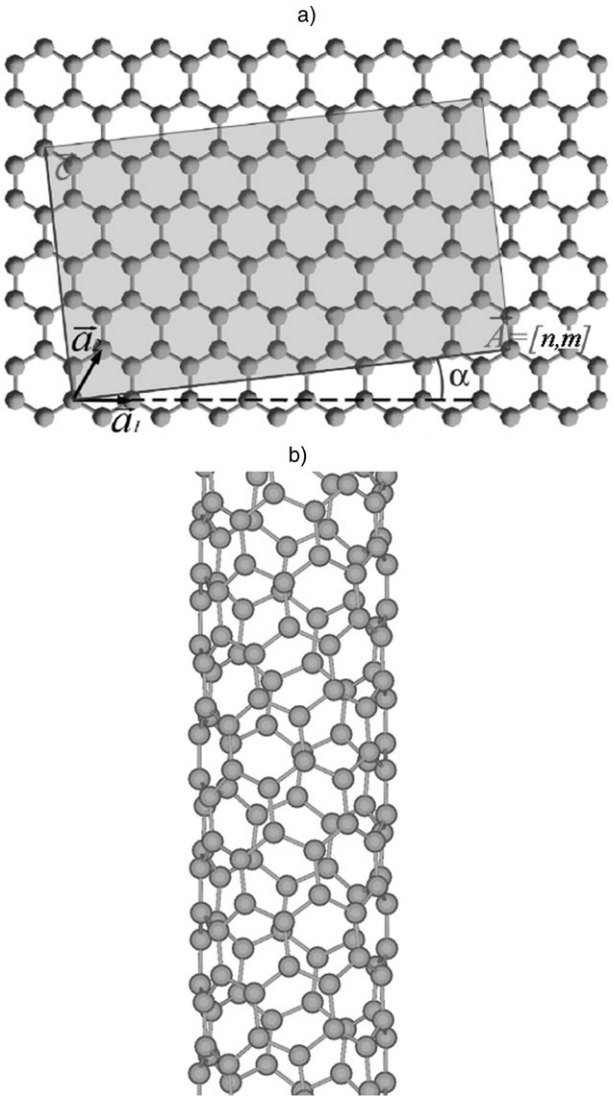

Fig. 1 (a) Schematic structure of graphene with basis vectors $\vec{a}_1$ and $\vec{a}_2$. The shadowed rectangle is the radial projection of carbon nanotube (7,1) with perimeter $\vec{A}$ and helical angle α. (b) Single-walled carbon nanotube (7,1) is formed from the cut by rolling it up about axis $\vec{c}$ perpendicular to the perimeter vector $\vec{A}$.

and the axial periodicity, *c*, of carbon nanotube (*n*,*m*) can also be obtained[86]

$$c = a_0\sqrt{n_c^2 + m_c^2 + n_c m_c} = \frac{\sqrt{3}a_0}{M}\sqrt{n^2 + m^2 + nm} = \frac{\sqrt{3}A}{M}. \tag{6}$$

When a rectangle with sides *A* and *c* is cut out of the graphene and is then rolled up about the tubule axis, *c*, perpendicular to the perimeter, *A*, a cylindrical nanotube (7,1) is formed as shown in Fig. 1(b).

The atomic positions of a single-walled carbon nanotube can be conveniently expressed by the Cartesian coordinates (x_j, z_j) in the radial projection, where the nanotube is projected onto a rectangle with sides *A* and *c* as described above. In fact, the atomic structure of the carbon nanotube can be described

by pairs of parallel atomic helices. There are three equivalent molecular helices in a single-walled carbon nanotube. They are parallel to the directions of the basis vectors $\vec{a}_1$, $\vec{a}_2$, and $\vec{a}_3 = \vec{a}_2 - \vec{a}_1$, respectively. The three primary helices are indicated on the graphene net as shown in Fig. 2(a). Each helix consists of a pair of atomic helices, displaced by a translational vector. Within a repetition unit in the axial direction, there are m helix pairs parallel to $\vec{a}_1$, n helix pairs parallel to $\vec{a}_2$, and $n + m$ helix pairs parallel to $\vec{a}_3 = \vec{a}_2 - \vec{a}_1$. With respect to a chosen carbon atom located at the origin, there are $n + m$ atoms on the primary helix parallel to $\vec{a}_1$ and their coordinates are (*c.f.* Fig. 2(b))

$$\begin{cases} x_j^{(1,0)} = ja_0\cos(\alpha), \\ z_j^{(1,0)} = -ja_0\sin(\alpha), \end{cases} \quad j = 0,\ 1,\ 2, \ldots,\ n+m-1, \qquad (7)$$

and the atoms on the secondary helix are at

$$\begin{cases} x_j^{(1,1)} = x_j^{(1,0)} - \dfrac{a_0}{\sqrt{3}}\cos(30^\circ - \alpha), \\ \\ z_j^{(1,1)} = z_j^{(1,0)} - \dfrac{a_0}{\sqrt{3}}\sin(30^\circ - \alpha), \end{cases} \qquad (8)$$

$$j = 0,\ 1,\ 2, \ldots,\ n+m-1.$$

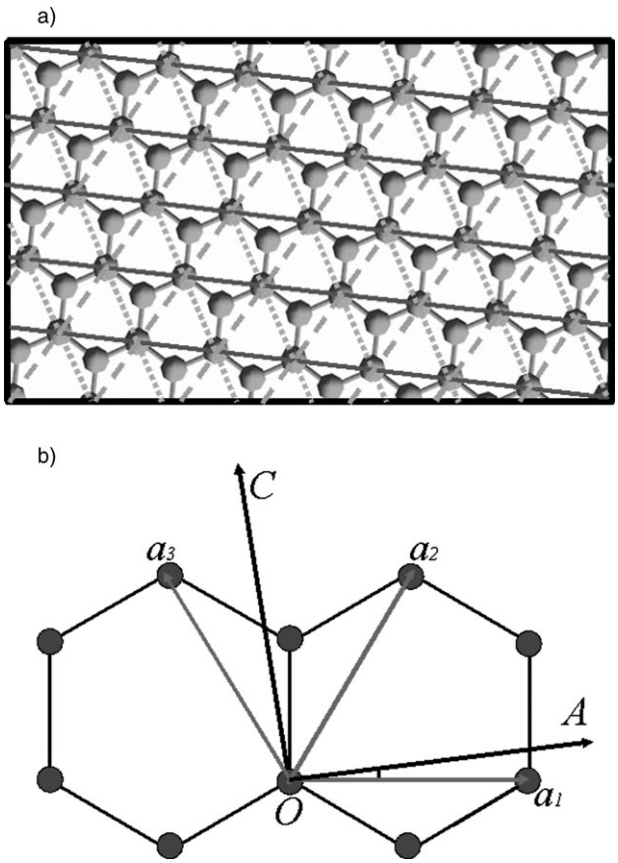

Fig. 2 (a) Schematic illustrating the principal helices that are parallel to the basis vectors $\vec{a}_1$ (solid), $\vec{a}_2$ (dashed) and $\vec{a}_3 = \vec{a}_2 - \vec{a}_1$ (dotted). (b) Definition of the chiral vector $\boldsymbol{A}$, axial direction $\boldsymbol{C}$, and the basis vectors $\vec{a}_1$, $\vec{a}_2$ and $\vec{a}_3 = \vec{a}_2 - \vec{a}_1$.

The atomic structure of the carbon nanotube can then be described by the m such helix pairs by translating the primary helix pair by multiples of the basis vector $\vec{a}_3$:

$$\begin{cases} x_j^{(3,0)} = -ja_0\sin(30^\circ - \alpha), \\ z_j^{(3,0)} = ja_0\cos(30^\circ - \alpha), \end{cases} \quad j = 0,\ 1,\ 2, \ldots,\ m-1. \qquad (9)$$

Similarly, the atomic positions on the primary helix parallel to $\vec{a}_2$ (left handed—the $\vec{c}$ axis is inverted in calculating the atomic coordinates) are

$$\begin{cases} x_j^{(2,0)} = ja_0\cos(60^\circ - \alpha), \\ \\ z_j^{(2,0)} = -ja_0\sin(60^\circ - \alpha), \end{cases} \qquad (10)$$

$$j = 0,\ 1,\ 2, \ldots,\ 2n-m-1.$$

and the atoms on the secondary helix are at

$$\begin{cases} x_j^{(2,1)} = x_j^{(2,0)} + \dfrac{a_0}{\sqrt{3}}\sin(\alpha) \\ \\ z_j^{(2,1)} = z_j^{(2,0)} - \dfrac{a_0}{\sqrt{3}}\cos(\alpha) \end{cases}, \qquad (11)$$

$$j = 0,\ 1,\ 2, \ldots,\ 2n-m-1.$$

The atomic structure of the carbon nanotube can be expressed by the n helix pairs generated by translating the primary helix pair by multiples of $\vec{a}_1$

$$\begin{cases} x_j^{(1,0)} = ja_0\cos(\alpha) \\ z_j^{(1,0)} = ja_0\sin(\alpha) \end{cases}, \ j = 0,\ 1,\ 2, \ldots,\ n-1. \qquad (12)$$

The atomic positions on the primary helix parallel to $\vec{a}_3 = \vec{a}_2 - \vec{a}_1$ are

$$\begin{cases} x_j^{(3,0)} = -ja_0\sin(30^\circ - \alpha) \\ \\ z_j^{(3,0)} = ja_0\cos(30^\circ - \alpha) \end{cases}, \qquad (13)$$

$$j = 0,\ 1,\ 2, \ldots,\ 2n+m-1.$$

and the secondary helix is

$$\begin{cases} x_j^{(3,1)} = x_j^{(3,0)} + \dfrac{a_0}{\sqrt{3}}\sin(30^\circ + \alpha) \\ \\ z_j^{(3,1)} = z_j^{(3,0)} - \dfrac{a_0}{\sqrt{3}}\cos(30^\circ + \alpha) \end{cases}, \qquad (14)$$

$$j = 0,\ 1,\ 2, \ldots,\ 2n+m-1.$$

The atomic structure of the carbon nanotube can be expressed by the $n + m$ helix pairs generated by translating the primary helix pair by multiples of $\vec{a}_1$

$$\begin{cases} x_j^{(1,0)} = ja_0\cos(\alpha) \\ z_j^{(1,0)} = -ja_0\sin(\alpha) \end{cases}, \ j = 0,\ 1,\ 2, \ldots,\ n+m-1. \qquad (15)$$

Due to the hexagonal rotational symmetry of the graphene lattice, the non-degenerate range for helicity, α, is 60°, which can be confined to the range of [0°,60°]. The values in [0°,30°] can be assigned to the right-handed tubules,

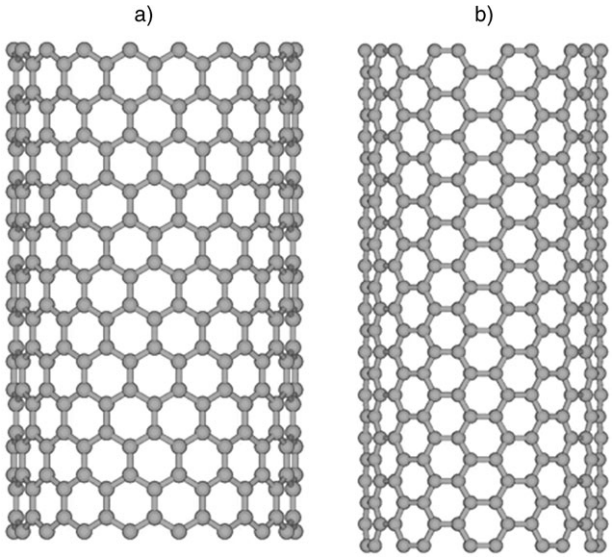

Fig. 3 (a) Carbon nanotube (18,0) (d = 1.409 nm and α = 0°) of zigzag structure; (b) nanotube (10,10) (d = 1.36 nm and α = 30°) of armchair structure.

while the values [30°,60°] are for the left-handed tubules. Among the three helices, two have the same handedness and the third has opposite handedness. Therefore, though the structure of carbon nanotubes is enantiomorphic, the choice of absolute handedness is arbitrary.

When the handedness of a tubule is ignored, the helical angle can be limited to [0°,30°]. Within this range, the chiral indices (n,m) are limited to values $n \geq m \geq 0$.

The rotational symmetry of a nanotube can be recognized by examining its chiral indices, (n,m). A carbon nanotube of indices (n,m) has N-fold rotational symmetry, with N being the greatest common divisor of n and m. When $m = 0$, the carbon nanotube possesses n-fold rotational symmetry, and it does not have a two-fold rotational symmetry when n is an odd number. On the other hand, when a two-fold axis is present, the carbon nanotube is also centrosymmetric.

There are two special non-helical structures that deserve special attention. One is the so-called zigzag structure, which has chiral indices of the form (n,0) with a helical angle $\alpha = 0°$, as shown in Fig. 3(a); the other is the armchair structure, which has indices of (n,n) with a helical angle α = 30°, shown in Fig. 3(b). In the zigzag structure, the tubule axis is $(n_c,m_c) = (-1, 2)$ and in the armchair structure it is $(n_c,m_c) = (-1, 1)$.

Diffraction from a continuous helix

The electron scattering amplitude can be expressed by the structure factor

$$F(\vec{q}) = \int V(\vec{r}) \exp(2\pi i \vec{q} \cdot \vec{r}) \mathrm{d}\vec{r}, \qquad (16)$$

where $V(\vec{r})$ is the modified scattering potential proportional to the Coulombic potential of the scattering object, $\vec{q}$ is the scattering vector ($q = 2\sin(\Theta/2)/\lambda$) with Θ and λ being the scattering angle and electron wavelength, respectively. The physically measurable diffraction intensity $I(\vec{q})$ in the reciprocal space is $I(\vec{q}) = |F(\vec{q})|^2$. For the general case of kinematical diffraction, where the Friedel's law holds, the diffraction intensity distribution is always centrosymmetric regardless of the symmetry of the scattering potential, *i.e.*, $I(-\vec{q}) = I(\vec{q})$. For a cylindrical object like a nanotube, it is more convenient to express the scattering amplitude in the polar coordinates (R, Φ, l) (*cf.* Appendix)

$$F(R,\Phi,l) = \frac{1}{c}\sum_{h=-\infty}^{+\infty} \exp\left[ih\left(\Phi+\frac{\pi}{2}\right)\right] \times \int_0^c \int_0^{2\pi} \int_0^{\infty} V(r,\phi,z) J_h(2\pi r R) \times \exp\left[i\left(-h\phi + \frac{2\pi l z}{c}\right)\right] r\mathrm{d}r\mathrm{d}\phi\mathrm{d}z, \qquad (17)$$

where $J_h(2\pi rR)$ is the Bessel function of integer order h and c is the structural periodicity of the tubular object in the direction of its unique axis (z-direction).

As an example to illustrate the scattering of helical structures, Fig. 4(a) shows a right-handed continuous helix of radius r_0 and pitch length C. The scattering potential can be expressed by

$$V(r,\phi,z) = V_0\delta(r-r_0)\delta\left(\frac{2\pi z}{C} - \phi\right) \qquad (18)$$

Using this potential, the scattering amplitude (17) becomes

$$F(R,\Phi,l) = r_0 V_0 J_l(2\pi r_0 R) \exp\left[i\left(\Phi+\frac{\pi}{2}\right)l\right], \qquad (19)$$

and the corresponding scattering intensity distribution is

$$I(R,\Phi,l) = |F(R,\Phi,l)|^2 = r_0^2 V_0^2 [J_l(2\pi r_0 R)]^2, \qquad (20)$$

which is plotted in Fig. 4(b).

There are two important characteristics in the Fraunhofer diffraction pattern of a helix that deserve special mention. One is that the intensity (eqn (20)) falls only on discrete lines (layer lines) indexed by integer l; the other is that the intensity on a layer line l is proportional to the square of the Bessel function of order l.

When there are two helices, shown schematically in Fig. 4(c), related by a twofold rotation axis, *i.e.*,

$$V(r,\phi,z) = V_0\delta(r-r_0) \times \left[\delta\left(\frac{2\pi z}{C} - \phi\right) + \delta\left(\frac{2\pi z}{C} - \phi + \pi\right)\right], \qquad (21)$$

the scattering amplitude then becomes

$$F(R,\Phi,l) = r_0 V_0 J_l(2\pi r_0 R) [1 + \exp(i\pi l)] \exp\left[i\left(\Phi+\frac{\pi}{2}\right)l\right], \qquad (22)$$

and the intensity distribution is

$$I(R,\Phi,l) = |F(R,\Phi,l)|^2 = \begin{cases} 4r_0^2 V_0^2 [J_l(2\pi r_0 R)]^2, l = \text{even}, \\ 0, \ l = \text{odd} \end{cases}. \qquad (23)$$

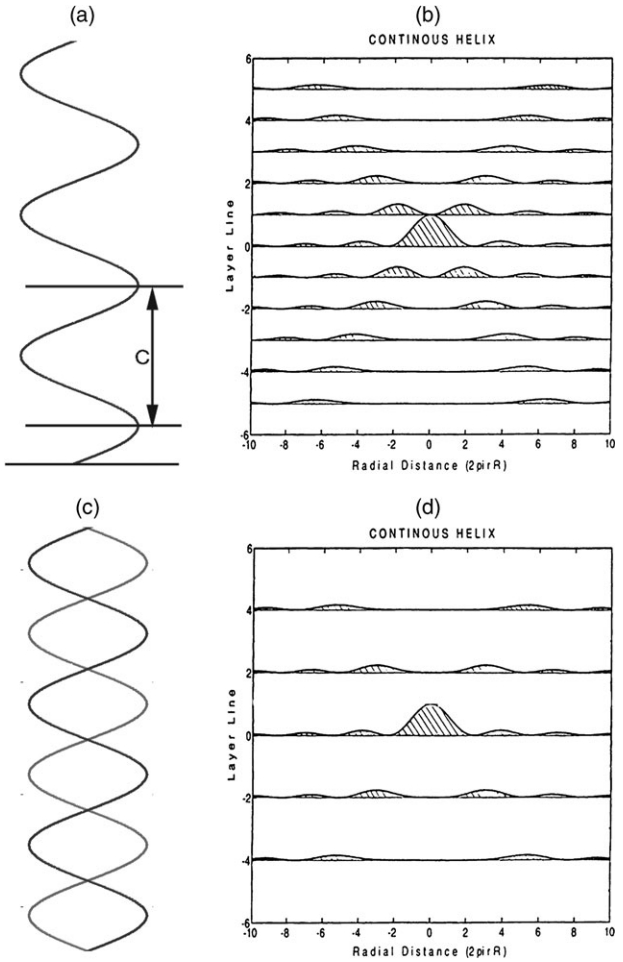

Fig. 4 (a) Schematic of a continuous helix of pitch length C. (b) Corresponding electron diffraction pattern of the continuous helix. It consists of a set of layer lines separated by $1/C$ and the intensity on layer line l is proportional to $|J_l(X)^2|$. (c) Two continuous helices with a phase difference of π and (d) the Fraunhofer diffraction pattern where the layer lines of odd indices are in extinction.

The layer lines of odd index l are in extinction, as shown in Fig. 4(d).

When there is an N-fold rotation axis, the layer lines will be in extinction except for those of indices equal to multiples of N. Correspondingly, the diffraction intensity on layer line of index $l = sN$ is proportional to $|J_{sN}(2\pi r_0 R)|^2$.

Electron diffraction from a nanotube

For a single-walled carbon nanotube of radius r_0, where the carbon atoms are located at discrete positions on a helix of radius r_0, as shown schematically in Fig. 5(a), the corresponding structure factor can be expressed as (*cf.* Appendix)

$$F(R,\Phi,l) = \sum_h \exp\left[ih\left(\Phi+\frac{\pi}{2}\right)\right] J_n(2\pi r_0 R) \times \sum_j f_j \exp\left[i\left(-h\phi_j + \frac{2\pi l z_j}{c}\right)\right], \quad (24)$$

where the summation for j is done over all atoms in a unit cell and h over all integers as allowed by the selection rule. This is a generic formula that is valid for all forms of nanotubes, elemental or composite.

The structure factor (eqn (24)) can also be rewritten as

$$F(R,\Phi,l) = \sum_h B_h(R,\Phi) T_{hl}, \quad (25)$$

where

$$B_h(R,\Phi) = \exp\left[ih\left(\Phi+\frac{\pi}{2}\right)\right] J_h(2\pi r_0 R), \quad (26)$$

and

$$T_{hl} = \sum_j f_j \exp\left[2\pi i\left(\frac{hx_j}{A}+\frac{lz_j}{c}\right)\right], \quad (27)$$

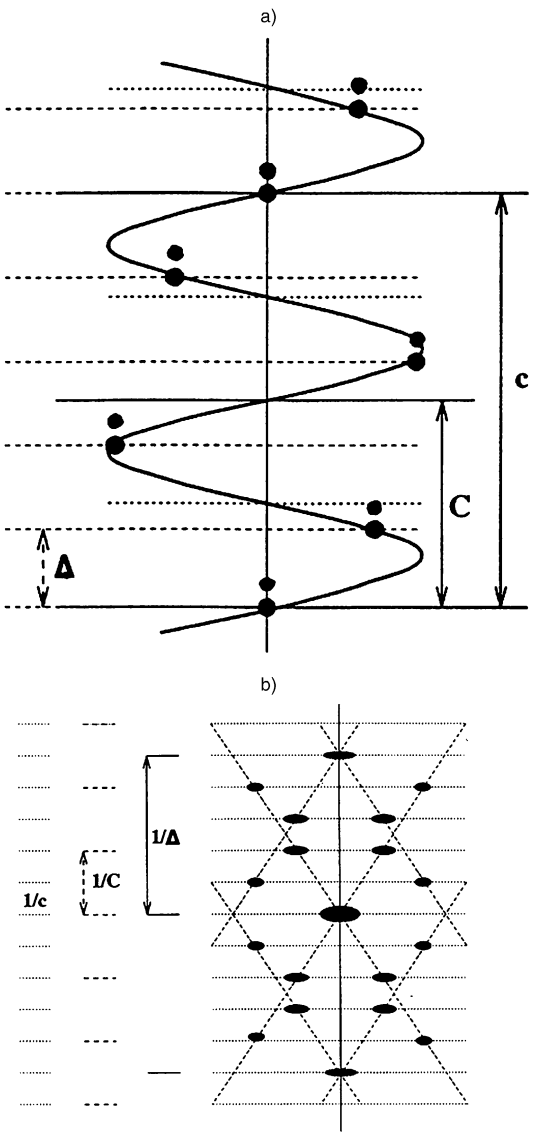

Fig. 5 (a) Schematic of a discontinuous helix where discrete groups of scatterers (atoms) are located on a helix of pitch length C. The periodicity of the structure and the separation between the neighboring molecular groups in the axial direction are given by c and Δ, respectively. (b) The corresponding Fraunhofer diffraction pattern.

with (x_j, z_j) being the atomic coordinates in radial projection in the horizontal and axial directions, respectively. Herewith, the diffraction effects from a cylindrical nanotube are more clearly seen by examining the two parts in eqn (25): (i) The structure factor in radial projection described by T_{hl}, which gives rise to the regular hexagonal diffraction pattern of graphene, and (ii) the modifying function $B_h(R, \Phi)$ that describes the effects of cylindrical curvature of the nanotube. The modifying Bessel functions produce streaks perpendicular to the tubule axis and also shift the diffraction intensity peak positions in the diffraction pattern. The shifts are dependent on the order of the operating Bessel functions.[39]

Selection rule for helix diffraction

When individual atoms are located on a continuous cylindrical helix, the scattering potential can be regarded as the product of the continuous helix and a set of equally spaced planes of spacing Δ, as illustrated in Fig. 5(a). The Fraunhofer diffraction from this structure can then be expressed by the convolution of the structure factor of the continuous helix and that of the equidistant planes. Since the latter is just a row of points located on the tubule axis with equal spacing $1/\Delta$, the final result is a set of diffraction patterns of the single continuous helix with origins located at each of the points on the tubule axis, as shown schematically in Fig. 5(b). Choosing c as the new structural periodicity along the tubule axis of a single helix and C as the pitch length of the continuous helix ($c \geq C$), then the allowed reflections on layer line l should satisfy

$$\frac{l}{c} = \frac{h}{C} + \frac{k}{\Delta}, \tag{28}$$

where k is an integer. For a given layer line l, the allowed orders of Bessel functions $J_h(2\pi r_0 R)$ are determined by combinations of h and all possible integers k that satisfy eqn (28). The selection rule (eqn (28)) can also be expressed equivalently as

$$l = ht + kp, \tag{29}$$

where $t = c/C$ gives the number of turns per unit periodicity in the axial direction and $p = c/\Delta$ gives the number of scattering units per complete period of the structure.

On the other hand, from the geometry in radial projection, for the atomic helices parallel to basis vector $\vec{a}_1$we have

$$\begin{cases} C = A\tan(\alpha) = a_0 \dfrac{m\sqrt{3(n^2+m^2+nm)}}{2n+m}, \\ \Delta = a_0 \sin(\alpha) = a_0 \dfrac{3m}{2\sqrt{3(n^2+m^2+nm)}}, \end{cases} \tag{30}$$

in terms of the chiral indices (n,m). The parameters t and p are then

$$\begin{cases} t = \frac{c}{C} = \dfrac{2n+m}{Mm}, \\ p = \frac{c}{\Delta} = \dfrac{2(n^2+m^2+nm)}{Mm}, \end{cases} \tag{31}$$

where M is the greatest common divisor of $(2n + m)$ and $(n + 2m)$. The selection rule for nanotube (n,m) can therefore also be expressed as

$$l = h\frac{2n+m}{Mm} + k\frac{2(n^2+m^2+nm)}{Mm}. \tag{32}$$

When the nanotube has rotational symmetry, the same selection rule applies if c is defined as the periodicity related to a specific helix. The additional rotational symmetry will lead to extinction layer lines. For a nanotube of N-fold rotational symmetry, only $l = sN(l = 0, \pm1, \pm2,\ldots)$ are allowed layer lines. Equivalently, this can be translated into additional constraints on the selection rule. If we use the structural periodicity, then the new periodicity will be shortened by N times to become c/N, and the selection rule (eqn (29)) $l = ht + kp$ will limit the values of h and k to be multiples of N, while l takes all possible integers.

It should also be noted that the selection rule given by eqn (32) is derived for the specific helix parallel to basis vector $\vec{a}_1$. When the structure of a carbon nanotube is expressed by other helices (helices parallel to $\vec{a}_2$ or $\vec{a}_3$), the corresponding selection rule will appear to be different in form for each of the helices, but they are actually equivalent to each other.

Structure factor of a carbon nanotube

To calculate the scattering amplitude for a single-walled carbon nanotube (n,m), it is more convenient to express its atomic structure by the atomic helix pairs parallel to the basis vectors $\vec{a}_1$, $\vec{a}_2$ and $\vec{a}_3 = \vec{a}_1 - \vec{a}_2$. For the m pairs of atomic helices parallel to $\vec{a}_1$ with atomic coordinates $(x_j^{(1,0)}, z_j^{(1,0)})$ and $(x_j^{(1,1)}, z_j^{(1,1)})$, where

$$\begin{cases} x_j^{(1,0)} = ja_0\cos(\alpha) \\ z_j^{(1,0)} = -ja_0\sin(\alpha) \end{cases}, \; j = 0,\ 1,\ 2,\ldots,\ n+m-1. \tag{33}$$

and

$$\begin{cases} x_j^{(1,1)} = x_j^{(1,0)} - \dfrac{a_0}{\sqrt{3}}\cos(30^\circ - \alpha) \\ z_j^{(1,1)} = z_j^{(1,0)} - \dfrac{a_0}{\sqrt{3}}\sin(30^\circ - \alpha) \end{cases}, \tag{34}$$
$$j = 0,\ 1,\ 2,\ldots,\ n+m-1.$$

the structure factor for the nanotube in radial projection is

$$\begin{aligned} T_{hl} &= \sum_j^{\text{atoms}} f\exp\left[2\pi i\left(\frac{hx_j}{A} + \frac{lz_j}{c}\right)\right] \\ &= f\sum_{s=0}^{m-1}\exp\left[2\pi i\left(\frac{hx_s^{(3,0)}}{A} + \frac{lz_s^{(3,0)}}{c}\right)\right] \\ &\times \sum_{j=0}^{n+m-1}\left\{\exp\left[2\pi i\left(\frac{hx_j^{(1,0)}}{A} + \frac{lz_j^{(1,0)}}{c}\right)\right]\right\} \\ &\times \left\{1 + \exp\left[-\frac{2\pi i a_0}{\sqrt{3}}\left(\frac{h\cos(30^\circ - \alpha)}{A} + \frac{l\sin(30^\circ - \alpha)}{c}\right)\right]\right\}. \end{aligned} \tag{35}$$

By inserting

$$\begin{cases} \cos(30^\circ - \alpha) = \dfrac{\sqrt{3}(n+m)}{2\sqrt{n^2+m^2+nm}} \\ \sin(30^\circ - \alpha) = \dfrac{n-m}{2\sqrt{n^2+m^2+nm}} \end{cases}, \tag{36}$$

and the selection rule for the $\vec{a}_1$ helices (eqn (32)) into eqn (35), we then have

$$\begin{aligned} T_{hl} &= (n+m)f\sum_{s=0}^{m-1}\left\{\exp\left[2\pi i\left(\frac{hx_s^{(1,0)}}{A}+\frac{lz_s^{(1,0)}}{c}\right)\right]\right\} \\ &\times\left\{1+\exp\left[-2\pi i\left(\frac{h+(n-m)k}{3m}\right)\right]\right\} \\ &= (n+m)f\sum_{s=0}^{m-1}\exp\left[2\pi is\frac{h+(n+m)k}{m}\right] \\ &\times\left\{1+\exp\left[-2\pi i\left(\frac{h+(n-m)k}{3m}\right)\right]\right\} \\ &= (n+m)f\frac{1-\exp\{2\pi i[h+(n+m)k]\}}{1-\exp[2\pi i[h+(n+m)k)/m]} \\ &\times\left\{1+\exp\left[-2\pi i\left(\frac{h+(n-m)k}{3m}\right)\right]\right\} \\ &= \begin{cases} m(n+m)f\left\{1+\exp\left[-2\pi i\left(\frac{h+(n-m)k}{3m}\right)\right]\right\} \\ \text{when } \frac{h+(n+m)k}{m} = N \text{ (integer).} \quad 0, \quad \text{otherwise} \end{cases}, \end{aligned} \tag{37}$$

The structure factor can therefore be expressed as

$$F_{nm}(R,\Phi,l) = \sum_{h,k} f\chi_{nm}(h,k)\gamma_{nm}(h,k)J_h(\pi dR)\exp\left[ih\left(\Phi+\frac{\pi}{2}\right)\right], \tag{38}$$

where

$$\chi_{nm}(h,k) = (n+m)\times\left\{1+\exp\left[-2\pi i\left(\frac{h+(n-m)k}{3m}\right)\right]\right\}, \tag{39}$$

which describes the scattering amplitude from a single helix pair parallel to $\vec{a}_1$, and

$$\gamma_{nm}(h,k) = \begin{cases} m, \text{ when}[h+(n+m)k]/m = N \text{ (integer)} \\ 0, \text{ otherwise} \end{cases}, \tag{40}$$

in which h, k and l are all integers that satisfy the selection rule for carbon nanotube (n,m) stipulated by eqn (32).

Visually, it is the helices that have the smallest angle with respect to the tubule axis that appear as the "helices". For this reason, we can also choose the helices parallel to $\vec{a}_2$ in the calculation of the structure factor. By inserting the atomic positions for carbon nanotube (n,m), the scattering amplitude (eqn (24)) becomes

$$F_{nm}(R,\Phi,l) = \sum_{h,k} f\chi_{nm}(h,k)\gamma_{nm}(h,k)J_h(\pi dR)\exp\left[ih\left(\Phi+\frac{\pi}{2}\right)\right], \tag{41}$$

where

$$\chi_{nm}(h,k) = (2n-m)\times\left\{1+\exp\left[-2\pi i\frac{h+(2n+m)k}{3n}\right]\right\}, \tag{42}$$

and

$$\gamma_{nm}(h,k) = \frac{1-\exp[2\pi i(h+mk)]}{1-\exp[2\pi i(h+mk)/n]} = \begin{cases} n, \text{ if } (h+mk)/n = N \\ 0, \text{ otherwise} \end{cases}, \tag{43}$$

in which m, n, and l are all integers that satisfy the same selection rule (eqn (29)) for carbon nanotube (n,m)

$$l = \frac{(n+2m)h+2(n^2+m^2+nm)k}{Mn}, \tag{44}$$

with M being the maximum common divisor of integers ($2n$ + m) and (n + $2m$). Eqn (44) is equivalent to eqn (32).

When the helices are counted in the direction of $\vec{a}_3$ = $\vec{a}_2 - \vec{a}_1$, then

$$F_{nm}(R,\Phi,l) = \sum_{h,k} f\chi_{nm}(h,k)\gamma_{nm}(h,k)J_h(\pi dR)\exp\left[ih\left(\Phi+\frac{\pi}{2}\right)\right], \tag{45}$$

where

$$\chi_{nm}(h,k) = (2n+m)\left\{1+\exp\left[2\pi i\frac{h-(n+2m)k}{3(n+m)}\right]\right\}, \tag{46}$$

and

$$\gamma_{nm}(h,k) = \frac{1-\exp[2\pi i(h-mk)]}{1-\exp[2\pi i(h-mk)/(n+m)]} = \begin{cases} n+m, \text{ if } (h-mk)/(n+m) = N \\ 0, \text{ otherwise} \end{cases}, \tag{47}$$

and the selection rule for the same carbon nanotube (n,m) appears as

$$l = \frac{(n-m)h+2(n^2+m^2+nm)k}{M(n+m)}, \tag{48}$$

which is equivalent to eqn (32) and (44).

The above equations are also valid for X-rays, when $V(\vec{r})$ and f are replaced by the electron charge density function, $\rho(\vec{r})$, and the atomic scattering amplitude for X-rays, $f^{(x)}$, respectively.

Electron diffraction from multi-walled carbon nanotubes

An ideal multi-walled carbon nanotube consists of multiple concentric shells with inter-tubular distances similar to the inter-planar spacings of graphite ($\sim$0.335 nm). The structure factor for a multi-walled carbon nanotube of N shells can be expressed as the coherent sum of the scattering amplitudes

from all individual shells in the multi-walled carbon nanotube[73]

$$F(R,\Phi,Z)=\sum_{j=1}^{N} f\delta(Z-\frac{l_j}{c_j})\sum_{h,k}\chi_j(h,k)\gamma_j(h,k)J_h(\pi d_j R)\times\exp\left[ih\left(\Phi+\frac{\pi}{2}\right)\right]\exp(i\varphi_j), \quad (49)$$

where j denotes the j-th nanotube (n_j,m_j) of axial periodicity c_j and diameter d_j, φ_j denotes the phase shift for the j-th shell relative to the reference shell in real space and

$$\chi_j(h,k)=(n_j+m_j)\left\{1+\exp\left[-2\pi i\frac{h+(n_j-m_j)k}{3m_j}\right]\right\}, \quad (50)$$

$$\gamma_j(h,k)=\frac{1-\exp[-2\pi i(h+(n_j+m_j)k)]}{1-\exp\left[-2\pi i\frac{h+(n_j+m_j)k}{m_j}\right]}=\begin{cases} m_j, & \text{if } \frac{h+(n_j+m_j)k}{m_j}=\text{ integer} \\ 0, & \text{otherwise}\end{cases}, \quad (51)$$

in which h, k and l_j are all integers governed by the selection rule for the j-th shell of the nanotube:

$$l_j=\frac{(2n_j+m_j)h+2(n_j^2+m_j^2+n_jm_j)k}{M_jm_j}, \quad (52)$$

with M_j being the maximum common divisor of $(2n_j + m_j)$ and $(n_j + 2m_j)$.

The electron diffraction intensity distribution is $I(R, \Phi, Z) = |F(R, \Phi, Z)|^2$.

As a special case, for electron diffraction from single-walled carbon nanotubes, the summation over j in eqn (49) disappears ($N = 1$) and so does the subscript j in eqn (50–52).

Principal layer lines

On the electron diffraction pattern of a single-walled carbon nanotube, the primary graphene reflections of Miller indices (10), (01), (11), $(\bar{1}0)$, $(0\bar{1})$, and $(\bar{1}\bar{1})$, are of the strongest intensity. These reflections form three pairs of layer lines (three layer lines above the equatorial line and three below the equatorial line), labelled l_1 (formed by the graphene (01) reflections), l_2 (formed by the graphene $(\bar{1}0)$ reflections) and l_3 (formed by the graphene (11) reflections) with respective layer line spacings D_1, D_2, and D_3 relative to the equatorial layer line. These three pairs of layer lines are referred to as the principal layer lines and are schematically illustrated in Fig. 6. It is experimentally most convenient to use these principal layer lines to characterize the carbon nanotube. Due to the very small diameter of carbon nanotubes, the diffraction peaks are elongated perpendicular to the tubule axis and only reflections close to the meridian have significant intensities. In some cases, the reflections $(1\bar{1})$ and $(\bar{1}1)$ are also used, which will be referred to in this article as layer line l_4 with layer line spacing D_4.

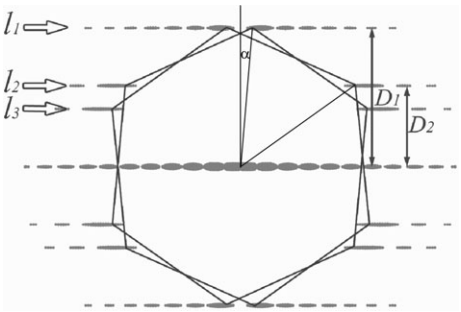

Fig. 6 Relationship between the principal graphene reflections (positioned at the six apices of the regular hexagons) and the principal layer line reflections l_1, l_2, and l_3 of a carbon nanotube. D_1 and D_2 are the respective layer line spacings. Spotty graphene reflections become streaks elongated in the directions perpendicular to the tubule axis. α is the helical angle of the nanotube.

Direct determination of chiral Indices (*n*,*m*)

It is important to note that, on each layer line, though the scattering amplitude is expressed by a summation of all Bessel functions that are allowed by the selection rule, there is usually only one order of Bessel function that dominates the intensity distribution on a particular layer line. All the others contribute negligibly to the layer line intensity. We can deduce the above conclusion from the selection rule. Under the constraints governed by the selection rule, all the possible values of h for one chosen layer line l can be expressed as follows[71]

$$h=h_0+\frac{2P(n^2+m^2+nm)}{M}, \quad (53)$$

where P are positive integers that also make h an integer, and h_0 defines the smallest non-negative integer for the chosen layer line l. Because $(n^2 + m^2 + nm)/M$ is always an integer,[79] $2P(n^2 + m^2 + nm)/M$ is usually a very large number. Since the magnitude of Bessel functions decreases significantly with the increase of their orders, the diffraction intensity on a particular layer line is essentially dominated by a single Bessel function of the lowest order h_0. For example, for single-walled carbon nanotube (14, 9) ($d = 1.572$ nm and $\alpha = 22.84°$), for the principal layer line $l_1(l = 37)$, $h_0 = 9$ and the next contributing Bessel function is $h_1 = 797$. The magnitude of the first peak for $|J_9(x)|^2$ is more than 20 times that for $|J_{797}(x)|^2$. Furthermore, the first peak position of $J_{797}(x)$ on the layer line l_1 is 75 times larger than that due to $J_9(x)$. Therefore, the diffraction intensity distribution on the layer line $l = 37$ for carbon nanotube (14,9) is only modulated by $|J_9(x)|^2$ within the range of collection where significant experimental data are present in the reciprocal space.

The order of the primary operating Bessel function for a given carbon nanotube (n,m) can be obtained by considering the crystallographic indices of the graphene reflections using the extended cell of the nanotube in radial projection, which is related to the index, h. In the Fraunhofer diffraction pattern of the graphene lattice, the allowed Bragg reflections are described by

$$\vec{g}=h_0\vec{a}_1^*+k_0\vec{a}_2^*. \quad (54)$$

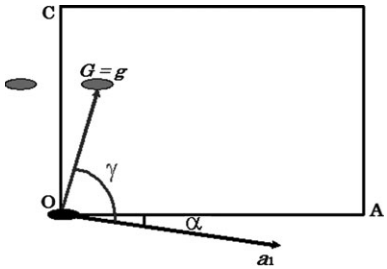

Fig. 7 Schematic assisting the deduction of the order of the operating Bessel function on a carbon nanotube of chiral indices (*n*,*m*). $\boldsymbol{a}_1$ is the basis vector and $\boldsymbol{g}$ refers to a particular reflection of interest. $\boldsymbol{A}$ is the perimeter vector and $\boldsymbol{C}$ is the axial vector of the nanotube. α is the helical angle of the nanotube and γ is the angle between vector $\boldsymbol{g}$ and the basis vector $\boldsymbol{a}_1$.

For a given nanotube of chiral indices (*n*,*m*), the corresponding nanotube reflections can also be indexed by the crystallographic indices (*h*,*l*) related to its radial projection net. Therefore, the selection rule should be such that the reflection $\vec{G} = h\vec{A}^* + l\vec{C}^*$ indexed using the radial projection net should fall onto the reciprocal lattice point $\bar{g}$ indexed using the graphene lattice, where $\vec{A}^*$ and $\vec{C}^*$ are the basis vectors of the reciprocal lattice of the radial projection net (rectangle with sides $\vec{A}$ and $\vec{C}$) of the nanotube:

$$\begin{cases} \vec{A}^* = \dfrac{1}{n^2+m^2+nm}(n\vec{a}_1 + m\vec{a}_2) \\ \vec{C}^* = \dfrac{1}{n_c^2+m_c^2+n_cm_c}(n_c\vec{a}_1 + m_c\vec{a}_2) \end{cases}. \tag{55}$$

The selection rule can then be written as

$$\vec{G} = \vec{g}, \tag{56}$$

or

$$h\vec{A}^* + l\vec{C}^* = h_0\vec{a}_1^* + k_0\vec{a}_2^*. \tag{57}$$

Multiplying both sides of eqn (57) by $\vec{a}_1$, we obtain

$$h\vec{A}^* \cdot \vec{a}_1 + l\vec{C}^* \cdot \vec{a}_1 = h_0, \tag{58}$$

or equivalently

$$\frac{ha_0\cos(\alpha)}{A} - lC^*\sin(\alpha) = h_0. \tag{59}$$

Note that [*cf*. Fig. 7]

$$lC^* = g\sin(\gamma - \alpha), \tag{60}$$

where γ is the angle between the basis vector $\vec{a}_1$ and the concerned graphene reflection (h_0k_0). We can then obtain the following relationship[39]

$$h = h_0n + k_0m, \tag{61}$$

As shown in Fig. 6, the three principal layer lines, l_1, l_2 and l_3, are formed by graphene reflections (01), ($\bar{1}$0), and (11), respectively. When choosing the reference graphene reflection as (01), *i.e.*, $h_0 = 0$ and $k_0 = 1$, the order of the dominating Bessel function is

$$h = m, \tag{62}$$

and for graphene reflection ($\bar{1}$0)

$$h = -n, \tag{63}$$

and for grapheme reflection (11)

$$h = n + m, \tag{64}$$

Therefore, the operating Bessel functions on the three principal layer lines, l_1, l_2, and l_3, are of orders m, $-n$, and $n + m$, respectively.

The order of the dominant Bessel function on each of the principal layer lines can also be understood by the formation of the electron diffraction pattern from the three principal helices that are parallel to $\vec{a}_1$, $\vec{a}_2$, and $\vec{a}_3 = \vec{a}_2 - \vec{a}_1$, respectively. The numbers of helix pairs are m, n, and $n + m$, respectively. From Fig. 6, one can see that the three principal layer lines, l_1, l_2, and l_3, correspond to these three helix pairs. Therefore, the first non-extinction reflections due to these three principal helices are expressed by the Bessel functions of order m, n, and $n + m$, respectively.

The same conclusion can also be reached algebraically from the selection rule.[79]

Therefore, the reflection intensities on the three principal layer lines, designated as layer lines l_1, l_2, and l_3 as shown in Fig. 6, are related to the chiral indices (*n*,*m*) by

$$I_{l1}(R) \propto |J_m(\pi dR)|^2, \tag{65}$$

$$I_{l2}(R) \propto |J_{-n}(\pi dR)|^2 = |J_n(\pi dR)|^2, \tag{66}$$

$$I_{l3}(R) \propto |J_{n+m}(\pi dR)|^2, \tag{67}$$

and

$$I_{l4}(R) \propto |J_{-(n-m)}(\pi dR)|^2 = |J_{n-m}(\pi dR)|^2, \tag{68}$$

The order h of Bessel function $J_h(X)$ can be determined by examining the positions of its peaks, which are unique to each order of Bessel function. An efficient and convenient means to determine the order h of Bessel function $J_h(X)$ is to examine the ratio X_2/X_1 of the positions of its first two peaks located at X_1 and X_2, respectively, or any other pair of peaks unique to this Bessel function. The chiral indices (*n*,*m*) can therefore be obtained directly by determining the order of Bessel function $J_m(X)$ and $J_n(X)$ with $X = \pi dR$ from the scattering intensity distribution on layer lines l_1 and l_2, whose intensities are proportional to $|J_m(\pi dR)|^2$ and $|J_n(\pi dR)|^2$, respectively. On an experimental electron diffraction pattern, the positions of the first two peaks, R_1 and R_2, can be measured and the ratio $R_2/R_1 = X_2/X_1$ is independent on the camera length of the electron microscope at which the electron diffraction pattern is acquired.

This method allows a rapid and accurate assignment of the chiral indices (*n*,*m*). From the electron diffraction pattern, the chiral indices m and n can be obtained by comparing the ratio $R_2/R_1 = X_2/X_1$ with the tabulated values given in Table 1 for Bessel functions of order up to $h = 30$. For Bessel functions $J_{18}(X)$ and $J_{19}(X)$, for example, the ratios of $X_2/X_1 = R_2/R_1$ are 1.266 and 1.256, respectively, and the difference is large enough to be identified unambiguously. Using our current method, we can obtain the peak positions with a precision of

Table 1 Ratio of the second and the first peak positions of Bessel functions

n	X_2/X_1	n	X_2/X_1	n	X_2/X_1
1	2.892	11	1.373	21	1.239
2	2.197	12	1.350	22	1.232
3	1.907	13	1.332	23	1.226
4	1.751	14	1.315	24	1.218
5	1.639	15	1.301	25	1.211
6	1.565	16	1.287	26	1.206
7	1.507	17	1.275	27	1.201
8	1.465	18	1.266	28	1.196
9	1.428	19	1.256	29	1.192
10	1.398	20	1.247	30	1.188

0.3%, which allows us to assign the chiral indices unambiguously up to index 30 or nanotube diameter up to 4 nm.

Instead of using the positions of the first two peaks, other variations of this method have also been used to obtain the order of the operating Bessel functions.[84]

For non-helical nanotubes, *i.e.*, zigzag and armchair nanotubes with chiral indices $(n,0)$ and (n,n), respectively, overlap of the principal layer lines occurs. For a zigzag nanotube of indices $(n,0)$, layer lines l_2 and l_3 overlap with each other and its first principal layer line (l_1) has an intensity distribution proportional to $|J_0(\pi dR)|^2$ and the second layer line (l_2) has intensity proportional to $|J_n(\pi dR)|^2$. For an armchair nanotube (n,n), the first layer line l_1 and the second line l_2 overlap with intensities proportional to $|J_n(\pi dR)|^2$ and layer line l_3 falls on the equatorial line.

The major sources of error of this direct method are (i) low signal/noise ratio due to the small number of atoms in the scattering carbon nanotube and (ii) the identification of the peak positions in the intensity distribution on the principal layer lines. The signal/noise ratio can be enhanced by applying longer exposure in acquiring the experimental electron diffraction pattern.

The above conclusions are valid only for normal incidence, *i.e.*, the incident electron beam is perpendicular to the nanotube axis. When the nanotube deviates from this normal incidence by an angle β, illustrated schematically in Fig. 8, corrections are needed for the deduction of the order of the operating Bessel function. For an incident electron beam with an inclination angle β, the structure factor becomes[71]

$$F_{nm}(R,\Phi,l) = \sum_{h,k} f\chi_{nm}(h,k)\gamma_{nm}(h,k) \times J_h\left(\pi d\sqrt{R^2+\left(\frac{l\tan\beta}{c}\right)^2}\right)\exp\left[in\left(\Phi+\frac{\pi}{2}\right)\right]. \quad (69)$$

When the tilt is taken into account, the chiral indices (n,m) can still be derived using the direct method with a high accuracy even when the nanotube is not oriented normal to the incident electron beam.[85]

Ratio of chiral indices m/n

Since the atomic structure of carbon nanotube (n,m) is periodic in the axial direction, the layer lines are sharp and the respective layer line spacings, D_1, D_2, and D_3, can be measured

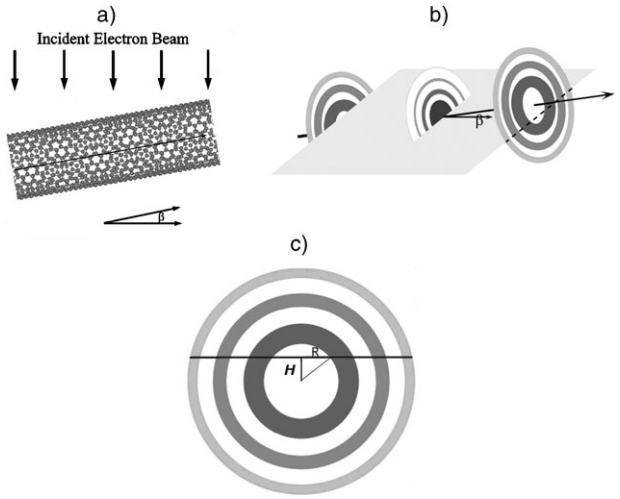

Fig. 8 (a) Geometric relationship in electron diffraction from a carbon nanotube when it is inclined by an angle, β, to the normal to the nanotube axis. (b) Corresponding relationship in the reciprocal space where the reflection intensities due to the nanotube are a set of concentric halo rings equally spaced in the axial direction. (c) Cross-sectional view of the diffraction in the reciprocal space, where the diffraction plane intercepts the intensity halo rings. The observed separation R on an experimental diffraction pattern is smaller than the maximum value observed at $\beta = 0°$. H is the vertical height of the intercept measured from the center of the intensity rings.[71]

accurately from the electron diffraction patterns. Although the cylindrical curvature of the nanotube causes severe distortion to the otherwise hexagonal electron diffraction pattern, the layer line spacings will not change due to the cylindrical curvature. The axial distances to the equatorial line, D_1, D_2, D_3 and D_4, of the fundamental reflections that form the principal layer lines can be calculated using the trigonometric relations illustrated schematically in Fig. 6, where α is the helical angle which is measured between the axial direction and the graphene (01) reflection in the reciprocal space

$$\begin{cases} D_1 = a^*\cos(\alpha) \\ D_2 = a^*\cos(60° - \alpha) \\ D_3 = a^*\cos(60° + \alpha) \\ D_4 = \sqrt{3}a^*\cos(30° - \alpha) \end{cases} \quad (70)$$

The layer line spacings are also related by

$$\begin{cases} D_1 = D_2 + D_3 \\ 2D_1 = D_2 + D_4 \end{cases}. \quad (71)$$

The helical angle, α, can be deduced from the ratio of the layer line spacings[45]

$$\alpha = \tan^{-1}\left(\frac{2D_2 - D_1}{\sqrt{3}D_1}\right). \quad (72)$$

The ratio of the chiral indices m and n can be obtained by inserting eqn (3) into eqn (70)[88]

$$\frac{m}{n} = \frac{2D_2 - D_1}{2D_1 - D_2}. \quad (73)$$

When the principal layer line spacings D_1 and D_3 are measured, for example, in terms of these two layer line spacings,

Table 2 List of m/n ratio, chiral indices (n,m), diameter (d), and helicity (α) of carbon nanotubes

m/n	n	m	d(n,m)	α	m/n	n	m	d(n,m)	α	m/n	n	m	d(n,m)	α	m/n	n	m	d(n,m)	α
0.0000	u	0		0.000	0.1538	13	2	1.105	7.053	0.2759	29	8	2.640	11.857	0.4000	5	2	0.489	16.102
0.0333	30	1	2.389	1.626	0.1538	26	4	2.209	7.053	0.2778	18	5	1.641	11.927	0.4000	10	4	0.978	16.102
0.0345	29	1	2.311	1.682	0.1579	19	3	1.618	7.223	0.2800	25	7	2.282	12.008	0.4000	15	6	1.467	16.102
0.0357	28	1	2.233	1.740	0.1600	25	4	2.132	7.311	0.2857	7	2	0.641	12.216	0.4000	20	8	1.956	16.102
0.0370	27	1	2.154	1.804	0.1667	6	1	0.513	7.589	0.2857	14	4	1.282	12.216	0.4000	25	10	2.445	16.102
0.0385	26	1	2.076	1.872	0.1667	12	2	1.027	7.589	0.2857	21	6	1.923	12.216	0.4000	30	12	2.934	16.102
0.0400	25	1	1.998	1.945	0.1667	18	3	1.540	7.589	0.2857	28	8	2.564	12.216	0.4074	27	11	2.652	16.337
0.0417	24	1	1.920	2.024	0.1667	24	4	2.054	7.589	0.2917	24	7	2.205	12.432	0.4091	22	9	2.163	16.390
0.0435	23	1	1.841	2.111	0.1667	30	5	2.567	7.589	0.2941	17	5	1.564	12.520	0.4118	17	7	1.674	16.474
0.0455	22	1	1.763	2.204	0.1724	29	5	2.490	7.827	0.2963	27	8	2.487	12.598	0.4138	29	12	2.859	16.537
0.0476	21	1	1.685	2.307	0.1739	23	4	1.976	7.889	0.3000	10	3	0.923	12.730	0.4167	12	5	1.185	16.627
0.0500	20	1	1.607	2.419	0.1765	17	3	1.463	7.994	0.3000	20	6	1.846	12.730	0.4167	24	10	2.370	16.627
0.0526	19	1	1.528	2.543	0.1786	28	5	2.412	8.080	0.3000	30	9	2.770	12.730	0.4211	19	8	1.881	16.764
0.0556	18	1	1.450	2.680	0.1818	11	2	0.949	8.213	0.3043	23	7	2.129	12.885	0.4231	26	11	2.577	16.826
0.0588	17	1	1.372	2.833	0.1818	22	4	1.899	8.213	0.3077	13	4	1.205	13.004	0.4286	7	3	0.696	16.966
0.0625	16	1	1.294	3.004	0.1852	27	5	2.335	8.350	0.3077	26	8	2.411	13.004	0.4286	14	6	1.392	16.966
0.0667	15	1	1.216	3.198	0.1875	16	3	1.365	8.445	0.3103	29	9	2.693	13.098	0.4286	21	9	2.088	16.996
0.0667	30	2	2.431	3.198	0.1905	21	4	1.821	8.565	0.3125	18	5	1.488	13.174	0.4286	28	12	2.784	16.966
0.0690	29	2	2.353	3.304	0.1923	26	5	2.257	8.639	0.3158	19	6	1.770	13.289	0.4333	30	13	2.991	17.142
0.0714	14	1	1.137	3.418	0.2000	5	1	0.436	8.948	0.3182	22	7	2.052	13.373	0.4348	23	10	2.295	17.187
0.0714	28	2	2.275	3.418	0.2000	10	2	0.872	8.948	0.3200	25	8	2.335	13.436	0.4375	16	7	1.599	17.269
0.0741	27	2	2.197	3.540	0.2000	15	3	1.308	8.948	0.3214	28	9	2.617	13.486	0.4400	25	11	2.502	17.345
0.0769	13	1	1.059	3.670	0.2000	20	4	1.744	8.948	0.3333	3	1	0.282	13.898	0.4444	9	4	0.903	17.480
0.0769	26	2	2.119	3.670	0.2000	25	5	2.180	8.948	0.3333	6	2	0.565	13.898	0.4444	18	8	1.806	17.480
0.0800	25	2	2.040	3.811	0.2000	30	6	2.616	8.948	0.3333	9	3	0.847	13.898	0.4444	27	12	2.709	17.480
0.0833	12	1	0.981	3.963	0.2069	29	6	2.539	9.223	0.3333	12	4	1.129	13.898	0.4483	29	13	2.916	17.596
0.0833	24	2	1.962	3.963	0.2083	24	5	2.103	9.280	0.3333	15	5	1.412	13.898	0.4500	20	9	2.013	17.647
0.0870	23	2	1.884	4.128	0.2105	19	4	1.667	9.367	0.3333	18	6	1.694	13.898	0.4545	11	5	1.110	17.784
0.0909	11	1	0.903	4.307	0.2143	14	3	1.231	9.515	0.3333	21	7	1.976	13.898	0.4545	22	10	2.220	17.784
0.0909	22	2	1.806	4.307	0.2143	28	6	2.461	9.515	0.3333	24	8	2.259	13.898	0.4583	24	11	2.427	17.897
0.0952	21	2	1.728	4.502	0.2174	23	5	2.025	9.637	0.3333	27	9	2.541	13.898	0.4515	13	6	1.317	17.992
0.1000	10	1	0.825	4.715	0.2222	9	2	0.795	9.826	0.3333	30	10	2.823	13.898	0.4615	26	12	2.635	17.992
0.1000	20	2	1.650	4.715	0.2222	18	4	1.569	9.826	0.3448	29	10	2.747	14.290	0.4643	28	13	2.842	18.073
0.1000	30	3	2.475	4.715	0.2222	27	6	2.384	9.826	0.3462	26	9	2.465	14.335	0.4667	15	7	1.524	18.143
0.1034	29	3	2.397	4.869	0.2273	22	5	1.948	10.023	0.3478	23	8	2.183	14.392	0.4667	30	14	3.049	18.143
0.1053	9	2	1.572	4.950	0.2308	13	3	1.153	10.158	0.3500	20	7	1.900	14.465	0.4706	17	8	1.732	18.258
0.1071	28	3	2.319	5.033	0.2308	26	6	2.307	10.158	0.3529	17	6	1.618	14.564	0.4737	19	9	1.939	18.349
0.1111	9	1	0.747	5.209	0.2333	30	7	2.666	10.257	0.3571	14	5	1.336	14.705	0.4762	21	10	2.146	18.422
0.1111	18	2	1.494	5.209	0.2353	17	4	1.512	10.333	0.3571	28	10	2.672	14.705	0.4783	23	11	2.353	18.482
0.1111	27	3	2.241	5.209	0.2381	21	5	1.871	10.440	0.3600	25	9	2.389	14.800	0.4800	25	12	2.560	18.533
0.1154	26	3	2.163	5.397	0.2400	25	6	2.230	10.513	0.3636	11	4	1.053	14.921	0.4815	27	13	2.767	18.576
0.1176	17	2	1.416	5.496	0.2414	29	7	2.589	10.566	0.3636	22	8	2.107	14.921	0.4828	29	14	2.975	18.613
0.1200	25	3	2.085	5.559	0.2500	4	1	0.359	10.893	0.3667	30	11	2.878	15.021	0.5000	2	1	0.207	19.107
0.1250	8	1	0.669	5.818	0.2500	8	2	0.718	10.893	0.3684	19	7	1.825	15.079	0.5000	4	2	0.414	19.107
0.1250	16	2	1.338	5.818	0.2500	12	3	1.077	10.893	0.3704	27	10	2.596	15.143	0.5000	6	3	0.622	19.107
0.1250	24	3	2.007	5.818	0.2500	16	4	1.435	10.893	0.3750	8	3	0.771	15.295	0.5000	8	4	0.829	19.107
0.1304	23	3	1.929	6.053	0.2500	20	5	1.794	10.893	0.3750	16	6	1.542	15.295	0.5000	10	5	1.036	19.107
0.1333	15	2	1.260	6.178	0.2500	24	6	2.153	10.893	0.3750	24	9	2.314	15.295	0.5000	12	6	1.243	19.107
0.1333	30	4	2.520	6.178	0.2500	28	7	2.512	10.893	0.3793	29	11	2.803	15.436	0.5000	14	7	1.450	19.107
0.1364	22	3	1.851	6.309	0.2593	27	7	2.435	11.242	0.3810	21	8	2.031	15.490	0.5000	16	8	1.657	19.107
0.1379	29	4	2.443	6.376	0.2609	23	6	2.076	11.302	0.3846	13	5	1.260	15.608	0.5000	18	9	1.865	19.107
0.1429	7	1	0.591	6.587	0.2632	19	5	1.717	11.387	0.3846	26	10	2.520	15.608	0.5000	20	10	2.072	19.107
0.1429	14	2	1.182	6.587	0.2667	15	4	1.359	11.517	0.3889	18	7	1.749	15.746	0.5000	22	11	2.279	19.107
0.1429	21	3	1.774	6.587	0.2667	30	8	2.717	11.517	0.3913	23	9	2.238	15.824	0.5000	24	12	2.486	19.107
0.1429	28	4	2.365	6.587	0.2692	26	7	2.358	11.612	0.3929	28	11	2.727	15.874	0.5000	26	13	2.893	19.107
0.1481	27	4	2.287	6.812	0.2727	11	3	1.000	11.742						0.5000	28	14	2.900	19.107
0.1500	20	3	1.696	6.890	0.2727	22	6	1.999	11.742						0.5000	30	15	3.108	19.107
0.5172	29	15	3.034	19.591	0.6364	11	17	1.231	22.689	0.7500	4	3	0.476	25.285	0.8500	20	17	2.512	27.320
0.5185	27	14	2.827	19.626	0.6364	22	14	2.461	22.689	0.7500	8	6	0.953	25.285	0.8519	27	23	3.394	27.355
0.5200	25	13	2.619	19.667	0.6400	25	16	2.803	22.777	0.7500	12	9	1.429	25.285	0.8571	7	6	0.382	27.457
0.5217	23	12	2.412	19.715	0.6400	14	9	1.572	22.846	0.7500	16	12	1.905	25.285	0.8571	14	12	1.795	27.457
0.3238	21	11	2.205	19.773	0.6429	28	18	3.144	22.846	0.7500	20	15	2.382	25.285	0.8571	21	18	1.765	27.457
0.5263	19	10	1.996	19.842	0.6471	17	11	1.913	22.947	0.7500	24	18	2.858	25.286	0.8571	28	24	2.647	27.457
0.5294	17	9	1.791	19.927	0.6500	20	13	2.255	23.018	0.7500	28	21	3.334	25.285	0.8621	29	25	3.530	27.457
0.5333	15	8	1.584	20.034	0.6522	23	15	2.596	23.070	0.7500	24	18	2.858	25.285	0.8636	22	19	2.783	27.581
0.5333	30	16	3.167	20.034	0.6538	26	17	2.937	23.110	0.7586	29	22	3.469	25.469	0.8667	15	13	1.900	27.638
0.5357	28	15	2.960	20.099	0.6552	29	19	3.278	23.141	0.7600	25	19	2.993	25.498	0.8696	23	20	2.918	27.693
0.5385	13	7	1.376	20.174	0.6667	3	2	0.341	23.413	0.7600	25	19	2.993	25.498	0.8750	8	7	1.018	27.796
0.5385	26	14	2.753	20.174	0.6667	6	4	0.083	23.413	0.7619	21	16	2.517	25.539	0.8750	16	14	2.036	27.796
0.5417	24	13	2.546	20.260	0.6667	9	6	1.024	23.413	0.7647	17	13	2.040	25.598	0.8750	24	21	3.054	27.796
0.5455	11	16	1.169	20.363	0.6667	12	8	1.368	23.413	0.7667	30	23	3.605	25.639	0.8800	25	22	3.189	27.889

Table 2 (*continued*)

m/n	n	m	d(n,m)	α	m/n	n	m	d(n,m)	α	m/n	n	m	d(n,m)	α	m/n	n	m	d(n,m)	α
0.5455	22	12	2.339	20.363	0.6667	15	10	1.707	23.413	0.7692	13	10	1.564	25.693	0.8824	17	15	2.171	27.933
0.5500	20	11	2.132	20.485	0.6667	18	12	2.048	23.413	0.7692	26	20	3.128	25.693	0.8846	26	23	3.325	27.975
0.5517	29	16	3.094	20.531	0.6667	21	14	2.369	23.413	0.7727	22	17	2.652	25.767	0.8889	9	8	1.153	28.055
0.5556	9	5	0.962	20.633	0.6667	24	16	2.731	23.413	0.7778	9	7	1.088	25.872	0.8889	18	16	2.307	28.055
0.5556	18	10	1.924	20.633	0.6667	27	18	3.072	23.413	0.7778	18	14	2.176	25.872	0.8889	27	24	3.490	28.055
0.5556	27	15	2.887	20.633	0.6667	30	20	3.413	23.413	0.7778	27	21	3.264	25.872	0.8929	28	25	3.596	28.128
0.5600	25	14	2.680	20.751	0.6786	28	19	3.207	23.691	0.7778	27	21	3.264	25.872	0.8947	19	17	2.443	28.163
0.5625	16	9	1.717	20.817	0.6800	25	17	2.865	23.724	0.7826	23	18	2.787	25.972	0.8966	29	26	3.732	28.196
0.5652	23	13	2.472	20.889	0.6818	22	15	2.524	23.780	0.7857	14	11	1.699	26.037	0.9000	10	9	1.289	28.259
0.5667	30	17	3.228	20.927	0.6842	19	13	2.183	23.822	0.7857	28	22	3.399	26.037	0.9000	20	18	2J578	28.259
0.5714	7	4	0.755	21.052	0.6842	19	13	2.183	23.822	0.7857	28	22	3.399	26.037	0.9000	30	27	2.578	28.259
0.5714	14	8	1.510	21.052	0.6875	16	11	1.841	23.897	0.7895	19	15	2.311	26.114	0.9048	21	19	2.714	28.346
0.5714	21	12	2.265	21.052	0.6897	29	20	3.341	23.947	0.7917	24	19	2.923	26.189	0.9091	11	10	2.714	28.346
0.5714	28	16	3.021	21.052	0.6923	13	9	1.500	24.007	0.7931	29	23	3.534	26.189	0.9091	22	20	2.849	28.425
0.5769	26	15	2.814	21.195	0.6923	26	18	3.000	24.007	0.7931	29	23	3.534	26.189	0.9130	23	21	2.985	28.497
0.5789	19	11	2.058	21.247	0.6957	23	16	2.659	24.084	0.8000	5	4	0.612	26.329	0.9167	12	11	1.560	28.562
0.5833	12	7	1.303	21.361	0.7000	10	7	1.159	24.182	0.8000	10	8	1.223	26.329	0.9167	24	22	3.120	28.562
0.5833	24	14	2.606	21.361	0.7000	20	14	2.318	24.182	0.8000	15	12	1.835	26.329	0.9200	25	23	3.256	28.622
0.5862	29	17	3.155	21.435	0.7000	30	21	3.476	24.182	0.8000	20	16	2.446	26.329	0.9231	13	12	1.696	28.677
0.5882	17	10	1.851	21.487	0.7000	20	14	2.318	24.182	0.8000	25	20	3.058	26.329	0.9231	26	24	3.392	28.677
0.5909	22	13	2.399	21.555	0.7037	27	19	3.135	24.266	0.8000	30	24	3.669	26.329	0.9259	27	25	3.527	28.728
0.5926	27	16	2.948	21.398	0.7059	17	12	1.976	24.315	0.8000	30	34	3.669	26.329	0.9286	14	13	1.831	28.728
0.6000	5	3	0.548	21.787	0.7083	24	17	2.794	24.370	0.8077	26	21	3.193	26.485	0.9286	28	26	3.663	28.775
0.6000	10	6	1.096	21.787	0.7143	7	5	0.818	24.504	0.8095	21	17	2.582	26.522	0.9310	29	27	3.798	2S.819
0.6000	15	9	1.644	21.787	0.7143	14	10	1.635	24.504	0.8125	16	13	1.970	26.582	0.9333	15	14	1.967	28.859
0.6000	20	12	2.193	21.787	0.7143	21	15	2.453	24.504	0.8148	27	22	3.329	26.628	0.9333	30	28	3.934	28.859
0.6000	25	15	2.741	21.787	0.7143	28	20	3.270	24.504	0.8182	11	9	1.359	26.696	0.9375	16	15	2.103	28.933
0.6000	30	18	3.289	21.787	0.7143	21	15	2.453	24.504	0.8182	22	18	2.717	26.996	0.9412	17	16	2.238	28.998
0.6071	28	17	3.082	21.967	0.7200	15	18	2.929	24.631	0.8214	28	23	3.464	26.760	0.9444	18	17	2.374	29.055
0.6087	23	14	2.534	22.006	0.7222	18	13	2.111	24.680	0.8235	17	14	2.105	26.802	0.9474	19	18	2.509	29.106
0.6111	18	11	1.986	22.066	0.7241	29	21	3.405	24.722	0.8261	23	19	2.852	26.853	0.9500	20	19	2.645	29.152
0.6154	13	8	1.437	22.173	0.7273	11	8	1.294	24.791	0.8276	29	24	3.599	26.882	0.9524	21	20	2.781	29.193
0.6154	26	16	2.875	22.173	0.7273	22	16	2.588	24.791	0.8333	6	5	0.747	26.995	0.9545	22	21	2.916	29.231
0.6190	21	13	2.327	22.264	0.7308	26	19	3.064	24.888	0.8333	12	10	1.494	26.995	0.9565	23	22	3.052	29.265
0.6207	29	18	3.216	22.304	0.7333	15	11	1.770	24.924	0.8333	18	15	2.241	26.995	0.9583	24	23	3.187	29.296
0.6250	8	5	0.889	22.411	0.7333	30	22	3.540	24.924	0.8333	24	20	2.988	26.995	0.9600	25	24	3.323	29.325
0.6250	16	10	1.779	22.411	0.7368	19	14	2.246	25.001	0.8333	30	25	3.735	26.995	0.9615	26	25	3.459	29.351
0.6250	24	15	2.668	22.411	0.7391	23	17	2.723	25.050	0.8400	25	21	3.123	27.126	0.9630	27	26	3.594	29.376
0.6296	27	17	3.009	22.525	0.7391	23	17	2.723	25.050	0.8421	19	16	2.376	27.167	0.9643	28	27	3.730	29.399
0.6316	19	12	2.120	22.572	0.7407	27	20	3.199	25.085	0.8462	13	11	1.629	27.245	0.9655	29	28	3.866	29.420
0.6333	30	19	3.351	22.015						0.8462	26	22	3.259	27.245	0.9667	30	29	4.001	29.439
															1.0000	n	n		30.000

the index ratio becomes

$$\frac{m}{n} = \frac{D_1 - 2D_3}{D_1 + D_3}. \quad (74)$$

On the other hand, if the layer line spacings D_3 and D_4 are measured, then

$$\frac{m}{n} = 1 - \frac{3D_3}{D_4}. \quad (75)$$

In fact, when the layer line spacings D_1 and D_4 are accessible, the result would be most accurate by using the following calculation

$$\frac{m}{n} = \frac{3D_1}{D_4} - 2, \quad (76)$$

eqn (73–76) offer a complimentary, and sometimes a more convenient, method to determine the chiral indices (n,m) for the following reasons:

(i) The ratio m/n is independent of the camera length at which the electron diffraction pattern is taken;

(ii) The ratio is independent of the relative orientation between the nanotube and the incident electron beam;

(iii) When the signal/noise ratio is low, this ratio can still be conveniently obtained.

The use of eqn (73–76) can result in a very high accuracy. The indeterminancy arising from the uncertainties these equations leads to only the nanotube of the smallest diameter (n_0,m_0). Other nanotubes meeting the same equations have chiral indices that are multiples of (n_0,m_0), *i.e.*, (n,m) = (jn_0, jm_0), where j = 1, 2, 3, ... As can be seen from the possible indices, the largest uncertainty comes from the nanotubes of chiral indices of (2m, m), where the difference in diameter between the neighboring shells is 0.207 nm. This diameter difference can be discerned from other information such as the real-space electron micrographs. To aid the use of this method, Table 2 lists all possible m/n values for chiral indices up to (30,30).

Example 1: single-walled carbon nanotubes

The methods described above offer quick and accurate determination of the chiral indices of individual single-walled carbon nanotubes in experiments. In practice, in order to minimize radiation damage to the carbon nanotubes, it is

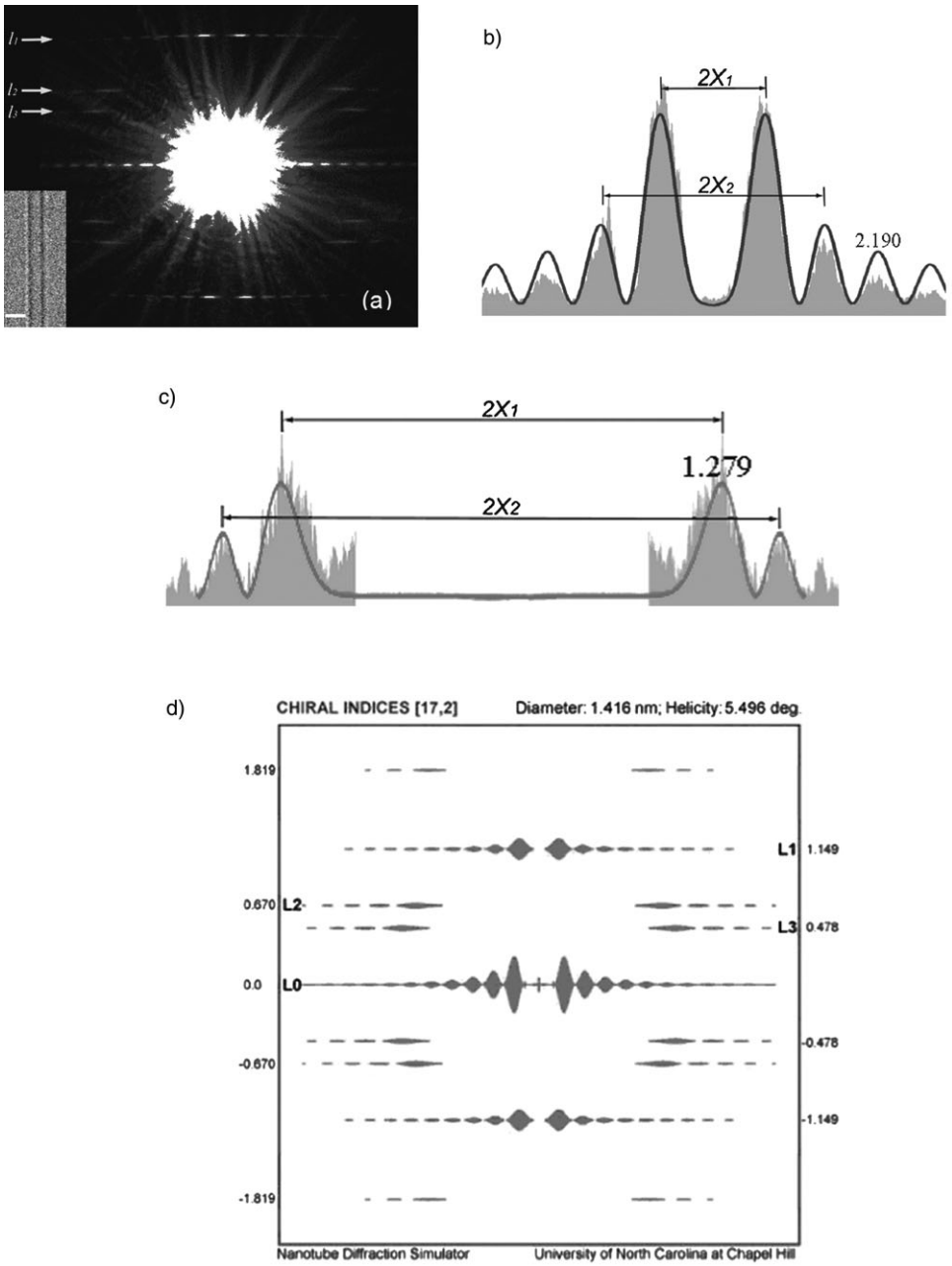

Fig. 9 (a) Electron diffraction pattern of carbon nanotube (17, 2). Inset is a high-resolution electron microscope image of the nanotube with a 2 nm scale bar. The three principal layer lines, l_1, l_2, and l_3, are indicated in the figure. (b) Intensity profile of principal layer line l_1. The ratio of the positions of the second peak (X_2) and the first peak (X_1) is 2.190, corresponding to $|J_2(X)|^2$, which is plotted as a solid line. (c) Intensity profile of principal layer line l_2. The ratio of the positions of the second peak (X_2) and the first peak (X_1) is 1.279, corresponding to the Bessel function $|J_{17}(X)|^2$, which is plotted as a solid line. The chiral indices of the nanotube are therefore (17, 2).[48] (d) Simulated electron diffraction pattern of nanotube (17, 2).

advisable to operate the transmission electron microscope at 80 kV. On the JEM-2010F TEM equipped with a field emission gun, the nanobeam electron diffraction patterns were acquired with a parallel beam of 20 nm spot size obtained with a smallest 10 μm condenser aperture and exciting the first condenser lens to maximum. The nanobeam electron diffraction patterns were recorded either directly with a CCD camera, or first on the photographic films, which were later scanned digitally to obtain more accurate measurement of the intensity distribution on the concerned layer lines. Fig. 9(a) shows a nanobeam electron diffraction pattern of a single-walled carbon nanotube of diameter $\sim$1.4 nm (a high-resolution electron microscope image is given as inset with 2 nm scale bar). From the intensity profiles on the three principal layer lines (l_1, l_2, and l_3), the ratios $R_2/R_1 = X_2/X_1$ on layer line l_1 and l_2 (Fig. 9(b) and (c)) were measured to be 2.200, and 1.279, respectively. The orders of the Bessel functions, and thus the chiral indices of the nanotube, were determined to be $m = 2$ and $n = 17$ (*cf.*, Table 1). The solid line profiles given in Fig. 9(b) and 9(c) are $|J_2(x)|^2$ and $|J_{17}(x)|^2$ (the intensity of

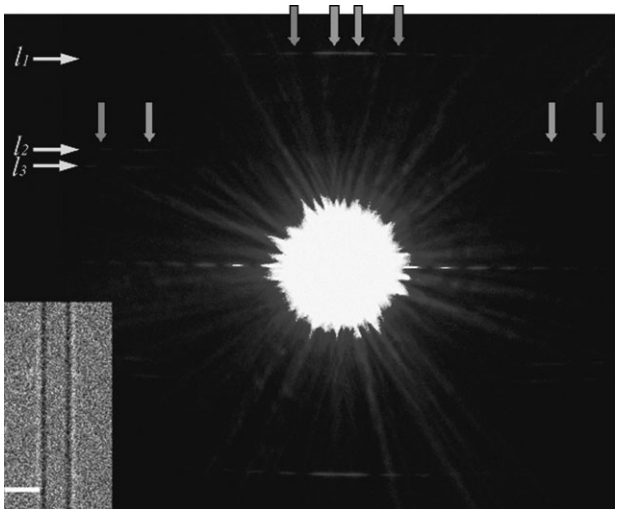

Fig. 10 Electron diffraction pattern of nanotube (17,1). Inset is an electron microscope image of the nanotube. The arrows point to the peak positions on layer line l_1 and l_2, respectively. The chiral indices of this nanotube was determined to be (17,1).[48]

Bessel functions of order 2 and 17, respectively) plotted on the experimental intensity data to illustrate the excellent agreement between the experimental intensity data and the intensity profile given by the Bessel function of single order. Nanotube (17, 2) is a metallic nanotube of diameter 1.418 nm and helicity 5.47°. Fig. 9(d) shows the calculated electron diffraction of the nanotube (17, 2), which again shows excellent agreement with the experimental data, as expected.

Fig. 10 shows the electron diffraction pattern obtained from another nanotube of similar diameter (image shown as inset with scale bar 2 nm). Using the same method, the chiral indices for this single-walled carbon nanotube were determined to be (17,1), which is a semiconducting tubule of diameter 1.374 nm and helicity 2.83°.

When the diameter of the nanotube is large, the ratio of X_2 and X_1 for a Bessel function is closer to that of its neighbors. In this case, layer lines l_3 (formed by the graphene (11) reflections) and/or l_4 (formed by the $(\bar{1}1)$ graphene reflections), whose intensity profiles correspond to $|J_{n+m}(\pi dR)|^2$ and $|J_{n-m}(\pi dR)|^2$, respectively, can be used as supplementary information to narrow down the choices and minimize the possible errors.

To improve the reliability and accuracy of the determination of the chiral indices (n,m), one should always apply both the direct measurement as well as the calculation of the index ratio m/n using the principal layer line spacings.

Given the experimental limitations, using the ratio of layer line spacings would give rise to results of highest accuracy. The major errors in the measurement of helicity come from the uncertainties in the measurement of the layer line spacings D_1 and D_2. In our current measurement, the errors of measuring D_1 and D_2 are 0.009 nm^{-1}. The errors in the deduction of the chiral indices are no larger than 0.2%.

Example 2: bundles of single-walled carbon nanotubes

Single-walled carbon nanotubes tend to form raft-like bundles when they are produced by laser evaporation or arc-discharge.[89–91] When they are packed in hexagonal closed packing, although their diameters are almost the same, it is not known if the helicity of all tubules are also the same, although theoretical arguments and the geometry seem to favor such a case.[89]

For a bundle of single-walled carbon nanotubes of the same diameter, the total scattering amplitude is the coherent sum of all individual contributions

$$F_T = \sum_j F_j(R, \Phi, l_j) \exp(2\pi i \delta_j), \qquad (77)$$

where δ_j is the phase shift caused by relative rotation and translation of the j-th nanotube relative to the reference nanotube. Given the weak bonding forces between the neighboring nanotubes, it is reasonable to assume that the above mentioned two degrees of freedom will make the scattering to a large extent incoherent. In this case, the resultant diffraction intensity distribution will be approximately equal to the sum of the individual scattering, in particular on the non-equatorial layer lines $l \neq 0$.

Fig. 11(a) shows a model structure of a raft-like bundle of single-walled carbon nanotubes. All nanotubes have similar diameter and are closed hexagonal packed. Fig. 11(b) is an electron micrograph of such a raft-like bundle of single-walled carbon nanotubes produced by single-beam laser evaporation.[90] There are about fifty nanotubes of about the same diameter in this bundle. Fig. 11(c) is an experimental electron diffraction pattern obtained from the bundle of nanotubes.[38] Letters A and Z indicate the positions of the reflection peaks from the armchair and zigzag nanotubes, respectively. The continuous distribution along the (10) and (11) reflection arcs are symmetrical about the tubule axis, indicating that the scattering tubules possess a rather uniform distribution of helicity. The electron diffraction can be calculated using a simplified model, as shown in Fig. 12(a). In this model, nine nanotubes of about the same diameter ($\sim$1.4 nm) are arranged in hexagonal closed packing. The electron diffraction intensity distribution is displayed in Fig. 12(b). As expected, the intensities are distributed rather evenly between the positions corresponding to the zigzag and the armchair structures.

Example 3: multi-walled carbon nanotubes

For a multi-walled carbon nanotube, it is necessary to determine the chiral indices (n_j,m_j) for each individual shell. In principle, while the methods detailed above are valid for multi-walled carbon nanotubes where the inter-layer interferences are not strong, due to the much larger diameter of multi-walled carbon nanotubes, complementary information such as eqn (72)–(76) is often very helpful to eliminate ambiguities. When the layer lines are read from the digitized data, the uncertainties in measuring the ratio m/n can be reduced to less than 0.2%. Once all the chiral indices are determined, the inter-tubular distances between the neighboring shells in the nanotube can also be obtained.

Fig. 13 shows an electron diffraction pattern of a double-walled carbon nanotube.[79] As can be seen from the pattern, there are now six pairs of principal layer lines across the equatorial layer line due to the two shells of the nanotube. The two sets of electron diffraction patterns are indicated by

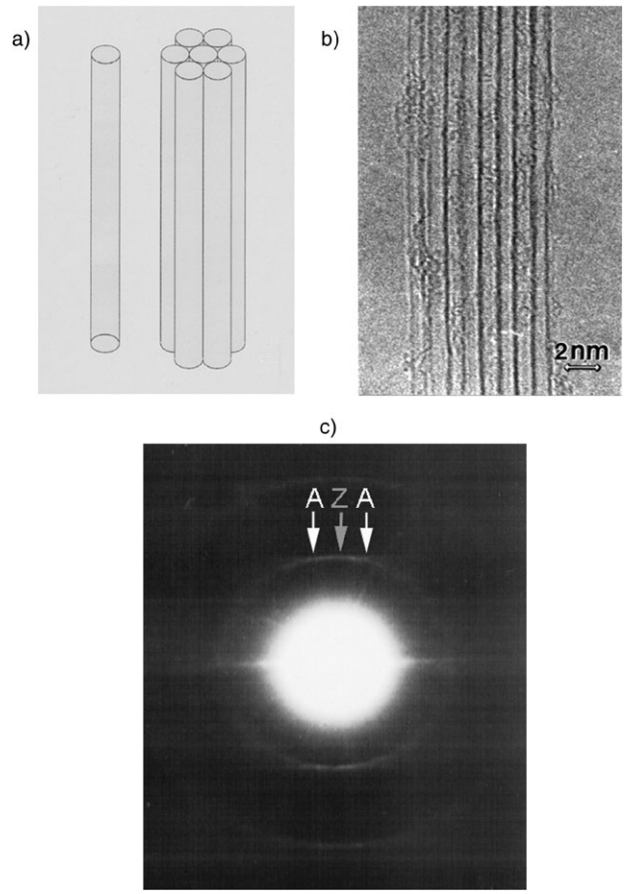

Fig. 11 (a) Structural model of a bundle of single-walled carbon nanotubes in closed hexagonal packing. (b) Electron microscope image of a bundle of raft-like single-walled carbon nanotubes. (c) Electron diffraction pattern of the bundle where the reflection intensities form continuous arcs. Letters A and Z indicate positions of reflection maxima due to the armchair and zigzag structures, respectively.[38]

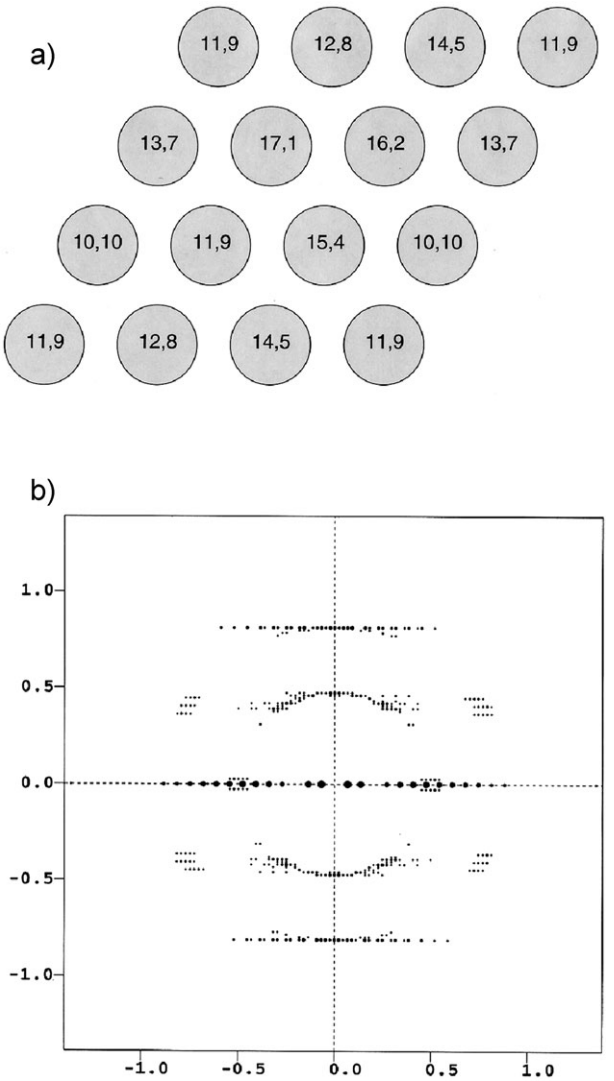

Fig. 12 (a) A model structure composed of nine carbon nanotubes of about the same diameter. The chiral indices of each nanotube are also given in the figure. (b) Calculated electron diffraction pattern of the model structure. Continuous distribution of scattering intensities is formed due to the rather uniform distribution of helicity in the nanotubes.[79]

arrows in the figure. The chiral indices of the two shells are determined to be (15,11) and (30,3), respectively. Their diameter and helicity are (1.770 nm, 24.92°) and (2.475 nm, 4.72°), respectively, with an inter-layer spacing of 0.355 nm.

Fig. 14 shows an electron diffraction pattern of a triple-walled carbon nanotube, where nine pairs of principal layer lines are present.[79] The chiral indices of the three shells are determined to be (35,14), (37,25), and (40,34), respectively. All three shells are metallic.

Fig. 15(a) shows the TEM image of a quadruple-walled carbon nanotube and the corresponding electron diffraction pattern of the nanotube is given in Fig. 15(b).[50] From the TEM image shown in Fig. 15(a), we can estimate that the nanotube has an inner diameter and outer diameter of 2.6 nm and 5.0 nm, respectively. The electron diffraction pattern of this carbon nanotube, a magnified portion of which is shown in Fig. 15(c), was used to deduce the chiral indices of each and every shell of the nanotube. It is also interesting to note that there are only three different helicities by examining the number of principal layer lines indicated by the arrows in the electron diffraction pattern due to the fact that two of the four shells have the same helicity. By measuring the principal layer line spacings in the electron diffraction pattern in Fig. 15(c), the m/n ratios were obtained as 0.031, 0.642, and 0.927, corresponding to helical angles 1.53°, 22.84°, and 28.76°, respectively. Using the principal layer line l_1 and the positions of the intensity peaks on this layer line, the value of index m can be deduced: $m = 25$ for the helicity of 22.84° and $m = 24$ for the helicity of 28.76°. Combining with the m/n ratios determined above, the chiral indices for these two nanotubes are assigned to be (26,24) and (39,25), respectively, which are neighboring shells in the nanotube.

Since there are four individual shells in the nanotube, two shells must have the same helicity. These two shells are identified by the modulations in the intensity distribution on the layer line marked with red arrows (helicity = 1.53°), which

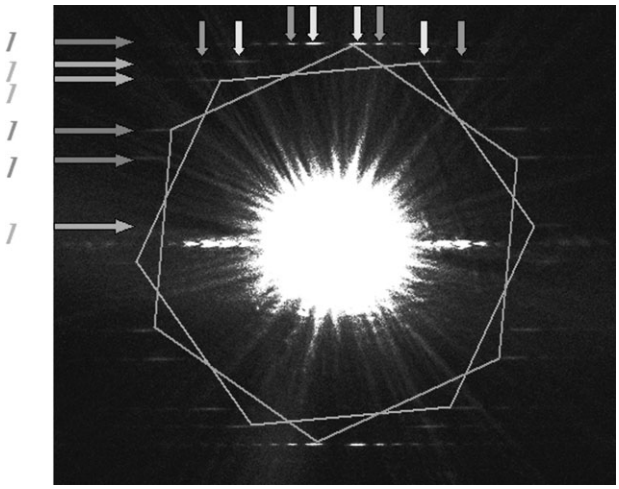

Fig. 13 Electron diffraction pattern of a double-walled carbon nanotube. Two sets of diffraction patterns, indicated by arrows, are identified. The chiral indices of the two shells of this nanotube are (15,11) and (30,3), respectively. Their diameter and helicity are (1.770 nm, 24.92°) and (2.475 nm, 4.715°), respectively.[79]

indicate that two nanotubes have both contributed to these layer lines and their chiral indices were determined to be (32,1) and (64,2), respectively, by making use of the geometric constraints of the concentric shells in the multi-walled carbon nanotube. Fig. 15(d) shows the determined structure in side view of the four shells of this nanotube with chiral indices (32,1), (26,24), (39,25) and (64,2), whose cross-sectional view is given in Fig. 15(e). All these shells are semiconducting. It is worth noting that the inter-tubular distances are not of the same value. They vary from 0.423 nm to 0.492 nm and to 0.358 nm from the outermost shell to innermost shell in the nanotube.

The procedure presented here for determining the atomic structure of the quadruple-walled carbon nanotube can be extended to multi-walled carbon nanotubes with fewer or more shells. With the precision given in the present measurement, up to nine shells (outer diameter up to 10 nm) have been determined unambiguously.[51] Once the atomic structure of a multi-walled carbon nanotube is determined, we can predict their physical and chemical properties, including identifying which shell is metallic or semiconducting.

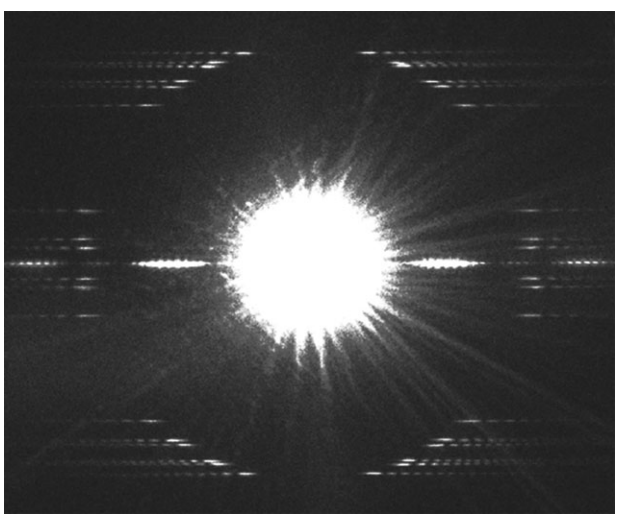

Fig. 14 Electron diffraction pattern of a triple-walled carbon nanotube. The pattern consists of three sets of individual patterns due to the three shells of the nanotube. The chiral indices of the three shells are determined to be (35,14), (37,25), and (40,34), respectively. All shells are metallic.[79]

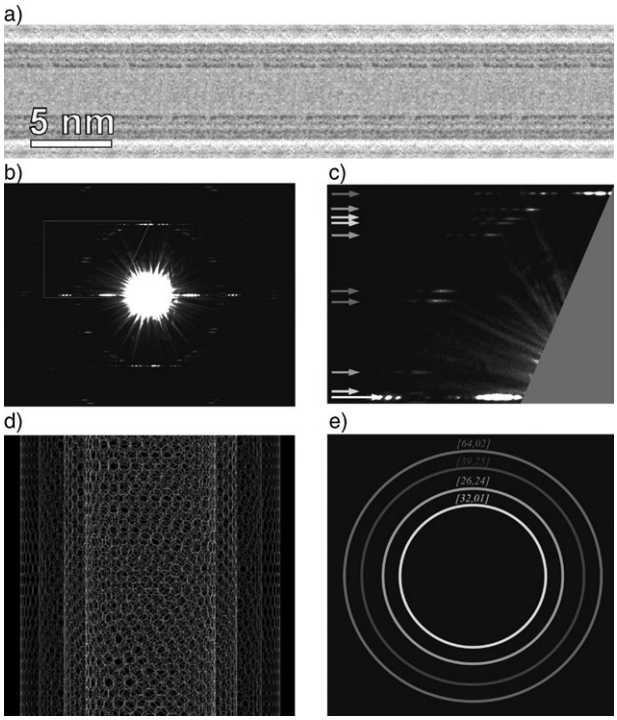

Fig. 15 (a) TEM image of a quadruple-walled carbon nanotube. (b) Corresponding electron diffraction pattern of the carbon nanotube. (c) Magnified portion of the diffraction pattern marked in (b). Only three sets of individual electron diffraction patterns can be identified due to the overlapping of the diffraction patterns of two of them, indicating that these two shells have the same helicity. (d) Side-view of the structure of the quadruple-walled carbon nanotube. (e) Cross-sectional view of the determined structure, where the chiral indices of each shell are also indicated.[50]

Conclusions

Rich information on the atomic structure is contained in the principal layer lines formed by the graphene reflections (01), ($\bar{1}$0), and (11) (l_1, l_2, and l_3 with respective layer line spacing D_1, D_2 and D_3) on an electron diffraction pattern of a carbon nanotube. The chiral indices of individual carbon nanotubes (n,m) can now be determined accurately using nano-beam electron diffraction. The diffraction intensities on the principal layer lines l_1, l_2, and l_3 are proportional to the square of the Bessel functions of orders m, n, and $n + m$: $I_{l1} \propto |J_m(\pi dR)|^2$, $I_{l2} \propto |J_n(\pi dR)|^2$, and $I_{l3} \propto |J_{n+m}(\pi dR)|^2$. By identifying the corresponding order of the Bessel function on the principal layer lines l_1 and l_2, the chiral indices (n,m) can be obtained. On the other hand, the ratio of the chiral indices can

be obtained with a high accuracy from the measurable layer line spacings $n/m = (2D_1 - D_2)/(2D_2 - D_1)$ and the chiral indices (n,m) could then be deduced with the aid of a chart.

Appendix

In a polar coordinate system, the coordinates (r, ϕ, z) are related to the Cartesian coordinates (x, y, z) by the following transformation

$$\begin{cases} x = r\cos(\phi) \\ y = r\sin(\phi) \\ z = z \end{cases}. \tag{A1}$$

For the coordinates in reciprocal space, the corresponding equations are

$$\begin{cases} X = R\cos(\Phi) \\ Y = R\sin(\Phi) \\ Z = Z \end{cases}. \tag{A2}$$

The structure factor in the polar coordinate system is

$$\begin{aligned} F(R,\Phi,Z) &= \int V(\vec{r})\exp(2\pi i\vec{q}\cdot\vec{r})\mathrm{d}\vec{r} \\ &= \int_{-\infty}^{+\infty}\int_0^{2\pi}\int_0^{\infty} V(r,\phi,z)\exp\{2\pi i[rR\cos(\phi-\Phi)+zZ]\}r\mathrm{d}r\mathrm{d}\phi\mathrm{d}z \\ &= \int_{-\infty}^{+\infty}\int_0^{2\pi}\int_0^{\infty} V(r,\phi,z)\exp[2\pi irR\cos(\phi-\Phi)]\exp(2\pi izZ)r\mathrm{d}r\mathrm{d}\phi\mathrm{d}z \end{aligned} \tag{A3}$$

and this is a general expression for any object in a polar coordinate system.

Introducing the Bessel function J_n of order n defined by

$$2\pi i^n J_n(u) = \int_0^{2\pi}\exp(iu\cos\phi + in\phi)\mathrm{d}\phi, \tag{A4}$$

and the following relationships:

$$\exp(iu\cos\phi) = \sum_{n=-\infty}^{+\infty} J_n(u)\exp\left[in\left(\phi+\frac{\pi}{2}\right)\right] \tag{A5}$$

$$J_{-n}(u) = (-1)^n J_n(u), \tag{A6}$$

we can obtain

$$\begin{aligned} F(R,\Phi,Z) &= \sum_n \int_{-\infty}^{+\infty}\int_0^{\infty} V(r,\phi,z)\exp(in\Phi) \\ &\times\left\{\int_0^{2\pi}\sum_{n=-\infty}^{+\infty} J_n(2\pi rR)\exp\left[in\left(\Phi-\phi+\frac{\pi}{2}\right)\right]d\phi\right\} \\ &\times\exp(2\pi izZ)r\mathrm{d}r\mathrm{d}\phi\mathrm{d}z \\ &= \sum_n \exp\left[in\left(\Phi+\frac{\pi}{2}\right)\right]\int_{-\infty}^{+\infty}\int_0^{2\pi}\int_0^{\infty} V(r,\phi,z)J_n(2\pi rR) \\ &\times\exp(-in\phi+2\pi izZ)r\mathrm{d}r\mathrm{d}\phi\mathrm{d}z. \end{aligned} \tag{A7}$$

When the potential $V(r, \phi, z)$ has an N-fold rotation axis along the z-direction, *i.e.*,

$$V(r,\phi,z) = V\left(r,\phi+\frac{2\pi}{N},z\right), \tag{A8}$$

the Fourier expansion of $V(r,\phi,z)$ can be written in the following form

$$V(r,\phi,z) = \sum_n V_{nN}(r,z)\exp(inN\phi), \tag{A9}$$

where

$$V_{nN}(r,z) = \frac{N}{2\pi}\int_0^{2\pi/n} V(r,\phi,z)\exp(-inN\phi)\mathrm{d}\phi, \tag{A10}$$

and the structure factor becomes

$$\begin{aligned} F(R,\Phi,Z) &= N\sum_{n=-\infty}^{+\infty}\exp\left[inN\left(\Phi+\frac{\pi}{2}\right)\right] \\ &\times\int_{-\infty}^{+\infty}\int_0^{2\pi}\int_0^{\infty} V(r,\phi,z)J_{nN}(2\pi rR) \\ &\times\exp(2\pi izZ)\exp(-inN\phi)r\mathrm{d}r\mathrm{d}\phi\mathrm{d}z. \end{aligned} \tag{A11}$$

If the object is periodic along the z-direction with periodicity c, the Fourier expansion (eqn (A4)) can be written as

$$V(r,\phi,z) = \sum_{n=-\infty}^{+\infty}\sum_{l=-\infty}^{+\infty} V_{nl}(r)\exp\left(-in\phi+\frac{2\pi ilz}{c}\right), \tag{A12}$$

and we can incorporate the z-components into the relevant equations to obtain the following expression of the structure factor:

$$\begin{aligned} F(R,\Phi,l) &= \frac{1}{c}\sum_{n=-\infty}^{+\infty}\exp\left[in\left(\Phi+\frac{\pi}{2}\right)\right] \\ &\times\int_0^{c}\int_0^{2\pi}\int_0^{\infty} V(r,\phi,z)J_l(2\pi rR)\exp\left[i\left(-n\phi+\frac{2\pi lz}{c}\right)\right]r\mathrm{d}r\mathrm{d}\phi\mathrm{d}z. \end{aligned} \tag{A13}$$

Acknowledgements

The author would like to thank his former graduate student, Dr. Zejian Liu, for his contributions, including preparation of many of the figures presented in this article, and Dr. Qi Zhang for her assistance. Financial support from the W.M. Keck Foundation, the University of North Carolina at Chapel Hill (UNC) and the UNC Research Council is also gratefully acknowledged.

References

1 W. H. Bragg and W. L. Bragg, *Nature*, 1913, **91**, 557.
2 W. H. Bragg and W. L. Bragg, *Proc. Roy. Soc. (London)*, 1913, **89A**, 277.
3 J. D. Bernal, *Proc. R. Soc. London, Ser. A*, 1924, **106**, 749.
4 H. W. Kroto, J. R. Heath, S. C. O'Brien, R. F. Curl and R. E. Smalley, *Nature*, 1985, **318**, 162.
5 W. Krätschmer, L. D. Lamb, K. Fostiropouls and D. R. Huffman, *Nature*, 1990, **347**, 354.
6 S. Iijima, *Nature*, 1991, **354**, 56.
7 Y. Ando and M. Ohkochi, *J. Cryst. Growth*, 1982, **60**, 147.

8 S. Iijima and T. Ichihashi, *Nature*, 1993, **363**, 603.
9 D. S. Bethune, C.-H. Kiang, M. S. de Vries, G. Gorman, R. Savoy, J. Vazquez and R. Beyers, *Nature*, 1993, **363**, 605.
10 A. M. Rao, E. Richter, S. Bandow, B. Chase, P. C. Eklund, K. A. Willams, S. Fang, K. R. Subbaswamy, M. Menon, A. Thess, R. E. Smalley, G. Dresselhaus and M. S. Dresselhaus, *Science*, 1997, **275**, 187.
11 A. Jorio, M. A. Pimenta, A. G. Souza, R. Saito, G. Dresselhaus and M. S. Dresselhaus, *New J. Phys.*, 2003, **5**, 139.
12 S. M. Bachilo, M. S. Strano, C. Kittrell, R. H. Huage, R. E. Smalley and R. B. Weisman, *Science*, 2002, **298**, 2361.
13 M. S. Strano, S. K. Doorn, E. H. Haroz, C. Kittrell, R. H. Huage and R. E. Smalley, *Nano Lett.*, 2003, **3**, 1091.
14 M. Ge and K. Sattler, *Science*, 1993, **260**, 515.
15 M. Ge and K. Sattler, *Appl. Phys. Lett.*, 1994, **65**, 2284.
16 N. Lin, J. Ding, S. Yang and N. Cue, *Carbon*, 1996, **34**, 1295.
17 J. W. G. Wildoer, L. C. Venema, A. G. Rinzler, R. E. Smalley and C. Dekker, *Nature*, 1998, **391**, 59.
18 T. W. Odom, J.-L. Huang, P. Kim and C. M. Lieber, *Nature*, 1998, **391**, 62.
19 W. Cochran, F. C. H. Crick and V. Vand, *Acta Crystallogr.*, 1952, **5**, 581.
20 J. D. Watson and F. C. H. Crick, *Nature*, 1953, **171**, 737.
21 M. H. F. Wilkins, A. R. Stokes and H. R. Wilson, *Nature*, 1953, **171**, 738.
22 R. Franklin and R. Gosling, *Nature*, 1953, **171**, 739.
23 A. Klug, F. H. C. Crick and H. W. Wyckoff, *Acta Crystallogr.*, 1958, **11**, 199.
24 B. K. Vainshtein, *Diffraction of X-Rays by Chain Molecules*, Elsevier Publishing, Amsterdam, 1966.
25 D. Sherwood, *Crystals, X-Rays and Proteins*, Longman, London, 1996.
26 L.-C. Qin, *J. Mater. Res.*, 1994, **9**, 2450.
27 A. A. Lucas, V. Bruyninckx and P. h. Lambin, *Europhys. Lett.*, 1996, **35**, 355.
28 P. Lambin and A. A. Lucas, *Phys. Rev.*, 1997, **B56**, 3571.
29 A. A. Lucas and P. Lambin, *Rep. Prog. Phys.*, 2005, **68**, 1181.
30 X. F. Zhang, X. B. Zhang, G. Van Tendeloo, S. Amelinckx, M. Op de Beeck and J. Van Landuyt, *J. Cryst. Growth*, 1993, **130**, 368.
31 X. B. Zhang, X. F. Zhang, S. Amelinckx, G. Van Tendeloo and J. Van Landuyt, *Ultramicroscopy*, 1994, **54**, 237.
32 X. B. Zhang and S. Amelinckx, *Carbon*, 1994, **32**, 1537.
33 S. Amelinckx, B. Devouard and A. Baronnet, *Acta Crystallogr.*, 1996, **A52**, 850.
34 D. Bernaerts, S. Amelinckx, P. Lambin and A. A. Lucas, *Appl. Phys. A: Mater. Sci. Process.*, 1998, **67**, 53.
35 S. Amelinckx, A. Lucas and P. Lambin, *Rep. Prog. Phys.*, 1999, **62**, 1471.
36 L.-C. Qin, T. Ichihashi and S. Iijima, *Ultramicroscopy*, 1997, **67**, 181.
37 J. M. Cowley, P. Nikolaev, A. Thess and R. E. Samlley, *Chem. Phys. Lett.*, 1997, **265**, 379.
38 L.-C. Qin, S. Iijima, H. Kataura, Y. Maniwa, S. Suzuki and Y. Achiba, *Chem. Phys. Lett.*, 1997, **268**, 101.
39 L.-C. Qin, *Chem. Phys. Lett.*, 1998, **297**, 23.
40 L.-C. Qin, *Mater. Characterization*, 2000, **44**, 407.
41 R. R. He, H. Z. Jin, J. Zhu, Y. J. Yan and X. H. Chen, *Chem. Phys. Lett.*, 1998, **298**, 170.
42 M. Kociak, K. Suenaga, K. Hirahara, Y. Saito, T. Nagahira and S. Iijima, *Phys. Rev. Lett.*, 2002, **89**, 155501.
43 J.-F. Colomer, L. Henrard, P. Lambin and G. Van Tendeloo, *Phys. Rev.*, 2001, **B64**, 125425.
44 J.-F. Colomer, L. Henrard, P. Lambin and G. Van Tendeloo, *Euro. Phys. J.*, 2002, **B27**, 111.
45 M. Gao, J. M. Zuo, R. D. Twesten, I. Petrov, L. A. Nagahara and R. Zhang, *Appl. Phys. Lett.*, 2003, **82**, 2703.
46 J.-F. Colomer, L. Henrard, P. Launois, G. Van Tendeloo, A. A. Lucas and P. Lambin, *Phys. Rev. B*, 2004, **70**, 075408.
47 J. M. Zuo, I. Vartanyants, M. Gao, R. Zhang and L. A. Nagahara, *Science*, 2003, **300**, 1419.
48 Z. Liu and L.-C. Qin, *Chem. Phys. Lett.*, 2005, **408**, 75.
49 Z. Liu, Q. Zhang and L.-C. Qin, *Phys. Rev. B*, 2005, **71**, 245413.
50 Z. Liu, Q. Zhang and L.-C. Qin, *Appl. Phys. Lett.*, 2005, **86**, 191903.
51 Q. Zhang, J. Tang, Z. Liu, H. Zhang, X. Zhao, Y. Ando and L.-C. Qin, *Proceedings of the 16th International Microscopy Congress*, 2006, p. 1312.
52 M. Liu and J. M. Cowley, *Carbon*, 1994, **32**, 393.
53 M. Liu and J. M. Cowley, *Ultramicroscopy*, 1994, **53**, 333.
54 X. D. Fan and L. A. Bursil, *Philos. Mag.*, 1995, **A72**, 139.
55 L. Margulis, P. Dluzewski, Y. Feldman and R. Tenne, *J. Microsc.*, 1996, **181**, 68.
56 D. Bernaerts, A. Zettl, N. G. Chopra, A. Thess and R. E. Smalley, *Solid State Commun.*, 1998, **105**, 145.
57 K. Hirahara, S. Bandow, K. Suenaga, H. Kato, T. Okazaki, H. Shinohara and S. Iijima, *Phys. Rev. Lett.*, 2000, **85**, 5384.
58 P. Lambin, V. Meunier, L. Henrard and A. A. Lucas, *Carbon*, 2000, **38**, 1713.
59 L. Henrard, A. Loiseau, C. Journet and P. Bernier, *Eur. Phys. J.*, 2000, **B13**, 661.
60 A. A. Lucas, F. Moreau and P. Lambin, *Rev. Mod. Phys.*, 2002, **74**, 1.
61 R. R. Schlittler, J. W. Seo, J. K. Gimzewski, C. Durkan, M. S. M. Saifullah and M. E. Welland, *Science*, 2001, **292**, 1136.
62 M. F. Chisholm, Y. H. Wang, A. R. Lupini, G. Eres, A. A. Puretzky, B. Brinson, A. V. Melechko, D. B. Geohegan, H. T. Cui, M. P. Johnson, S. J. Pennycook, D. H. Lowndes, S. C. Arepalli, C. Kittrell, S. Sivaram, M. Kim, G. Lavin, J. Kono, R. Hauge and R. E. Smalley, *Science*, 2003, **300**, 1236.
63 J. C. Meyer, M. Paillet, G. S. Duesberg and S. Roth, *Ultramicroscopy*, 2006, **106**, 76.
64 M. Kociak, K. Hirahara, K. Suenaga and S. Iijima, *Eur. Phys. J.*, 2003, **B32**, 457.
65 W. Ruland, A. K. Schaper, H. Hou and A. Greiner, *Carbon*, 2003, **41**, 423.
66 J.-F. Colomer, L. Henrard, G. Van Tendeloo, A. A. Lucas and P. Lambin, *J. Mater. Chem.*, 2004, **14**, 603.
67 G. Y. Zhang, X. Jiang and E. G. Wang, *Science*, 2003, **300**, 472.
68 (*a*) J. Luo, J. Zhu and H. Q. Ye, *Science*, 2004, **303**, 766c; (*b*) G. Y. Zhang, X. D. Bai, X. Jiang and E. G. Wang, *Science*, 2004, **303**, 766d.
69 K. Hirahara, S. Bandow, H. Kataura, M. Kociak and S. Iijima, *Phys. Rev. B*, 2004, **70**, 205422.
70 J. C. Meyer, M. Paillet, G. S. Duesberg and S. Roth, *Ultramicroscopy*, 2005, **106**, 176.
71 Z. Liu and L.-C. Qin, *Chem. Phys. Lett.*, 2004, **400**, 430.
72 Z. Liu and L.-C. Qin, *Chem. Phys. Lett.*, 2005, **402**, 202.
73 Z. Liu and L.-C. Qin, *Chem. Phys. Lett.*, 2005, **405**, 265.
74 Z. Liu and L.-C. Qin, *Chem. Phys. Lett.*, 2005, **406**, 106.
75 Z. Liu and L.-C. Qin, *Chem. Phys. Lett.*, 2005, **411**, 291.
76 Z. Liu and L.-C. Qin, *Chem. Phys. Lett.*, 2005, **412**, 399.
77 L.-C. Qin and S. Iijima, *Mater. Res. Soc. Symp. Proc.*, 2000, **593**, 33.
78 Z. Liu and L.-C. Qin, *Carbon*, 2005, **43**, 2146.
79 Z. Liu, PhD thesis, University of North Carolina at Chapel Hill, 2005.
80 J. C. Meyer, M. Paillet and S. Roth, *Science*, 2005, **309**, 1539.
81 J. Zhang and J. Zhu, *Chem. Phys. Lett.*, 2006, **420**, 171.
82 M. Y. Sfeir, T. Beetz, F. Wang, L. M. Huang, X. M. H. Huang, M. Y. Huang, J. Hone, S. O'Brien, J. A. Misewich, T. F. Heinz, L. J. Wu, Y. M. Zhu and L. E. Brus, *Science*, 2006, **312**, 554.
83 Z. Xu, X. D. Bai, Z. L. Wang and E. G. Wang, *J. Am. Chem. Soc.*, 2006, **128**, 1052.
84 H. Jiang, D. P. Brown, A. G. Nasibulin and E. I. Kauppinen, *Phys. Rev. B*, 2006, **74**, 035427.
85 H. Jiang, D. P. Brown, A. G. Nasibulin and E. I. Kauppinen, *Carbon*, 2006, DOI: 10.1016/j.carbon.2006.07.025.
86 R. Saito, G. Dresselhaus and M. S. Dresselhaus, *Physical Properties of Carbon Nanotubes*, Imperial College Press, London, 1998.
87 M. Abramovitz and I. A. Stegun, *Handbook of Mathematical Functions*, National Bureau of Standards, Washinton, DC, 1972.
88 L.-C. Qin, *Rep. Prog. Phys.*, 2006, **69**, 2761.
89 A. Thess, R. Lee, P. Nikolaev, H. J. Dai, P. Petit, J. Robert, C. H. Xu, Y. H. Lee, S. G. Kim, A. G. Rinzler, D. T. Colbert, G. E. Scuseria, D. Tomanek, J. E. Fischer and R. E. Smalley, *Science*, 1996, **273**, 483.
90 L.-C. Qin and S. Iijima, *Chem. Phys. Lett.*, 1997, **269**, 65.
91 C. Journet, W. K. Maser, P. Bernier, A. Loiseau, M. Lamy de la Chapelle, S. Lefrant, P. Deniards, R. Lee and J. E. Fischer, *Nature*, 1997, **388**, 756.

